



## RESEARCH ARTICLE

10.1029/2022JD036907

## Key Points:

- Competing ice nucleation processes in cirrus are predicted reliably and efficiently
- Partial activation of dust particles may occur frequently in cirrus formation
- Nucleation of ice within already-existing cirrus requires high updraft speeds

## Correspondence to:

B. Kärcher,  
[bernd.karcher@dlr.de](mailto:bernd.karcher@dlr.de)

## Citation:

Kärcher, B. (2022). A parameterization of cirrus cloud formation: Revisiting competing ice nucleation. *Journal of Geophysical Research: Atmospheres*, 127, e2022JD036907. <https://doi.org/10.1029/2022JD036907>

Received 8 APR 2022

Accepted 9 SEP 2022

## Author Contributions:

**Conceptualization:** B. Kärcher  
**Formal analysis:** B. Kärcher  
**Investigation:** B. Kärcher  
**Methodology:** B. Kärcher  
**Validation:** B. Kärcher  
**Writing – original draft:** B. Kärcher  
**Writing – review & editing:** B. Kärcher

# A Parameterization of Cirrus Cloud Formation: Revisiting Competing Ice Nucleation

B. Kärcher<sup>1</sup> <sup>1</sup>Institut für Physik der Atmosphäre, DLR Oberpfaffenhofen, Wessling, Germany

**Abstract** This study develops an advanced physically-based parameterization of heterogeneous ice nucleation in cirrus clouds that includes an updated parameterization of stochastic homogeneous freezing of supercooled solution droplets. Both components are formulated based on the same methodology and level of approximation, without numerical integration of the underlying ice supersaturation equation. The new scheme includes measured ice nucleation spectra describing deterministic ice activation from an arbitrary number of types of ice-nucleating particles (INPs), tracks the competition for available water vapor between the different ice nucleation modes, and allows for new ice formation and growth within pre-existing cirrus clouds. The computationally efficient scheme works with a minimal set of physical input parameters and predicts total nucleated ice crystal number concentrations (ICNCs) along with the maximum ice supersaturation attained during cirrus formation events. Aspects of its implementation into host models are discussed, including the provision of suitably parameterized vertical wind speeds. The parameterization is validated by comparisons to numerical simulations. First off-line applications to mineral dust and aviation soot particles are presented, including ICNC ensemble statistics resulting from the coupling with statistics of updraft speed variability.

**Plain Language Summary** Two decades after introduction of the first parameterization of cirrus cloud formation by freezing of ubiquitous liquid solution droplets, an improved version is developed based on the latest experimental findings regarding solid ice-nucleating particles, a small subset of the atmospheric aerosol. The new scheme allows to predict ice crystal formation in cirrus from competing homogeneous freezing and heterogeneous ice activation more realistically and with greater computational efficiency. It considers new developments regarding the properties of vertical wind speeds (triggering ice formation) and the molecular kinetics of water vapor uptake onto ice crystals (controlling ice growth). This study explains the foundation of cirrus ice formation and growth based on cloud physical theory, derives and explains the parameterization, discusses its use in host models to facilitate applications, checks its performance by comparison to comprehensive numerical simulations, and presents first results involving mineral dust and aircraft-emitted soot particles as examples for good and poor atmospheric ice-nucleating particles, respectively.

## 1. Introduction

Aerosol-cloud interactions challenge future climate change projections obtained with the help of global models. Initiation and development of the ice phase in atmospheric clouds is a long-standing, basic problem in cloud physics (Squires, 1967). In the case of pure ice (cirrus) clouds, competition between homogeneous solution droplet freezing and heterogeneous ice nucleation affects, if not controls, aerosol-cloud interactions (Kärcher, 2017a). The quest for better understanding aerosol effects in ice-containing clouds and representing them in global models is therefore a tall order. Due to the difficulty in directly capturing and resolving cloud microphysical processes and dynamical forcing of ice supersaturation in atmospheric measurements and global models, respectively, it is paramount to develop physically-based parameterizations of cloud ice formation, including effects of INPs. Such parameterizations are central components in the cloud schemes of atmospheric models (Morrison et al., 2020).

The nucleation of ice crystals from precursor aerosol particles is strongly coupled to depositional growth of the new phase by uptake of water vapor (H<sub>2</sub>O) molecules on the crystal surfaces. Aerosol particles compete during ice formation via the ice-supersaturated vapor. In contrast to purely data-driven approaches, physically-based parameterizations of ice formation are informed by laboratory experiments, in-situ observations, and cloud physical theory. However, the complexity of associated processes may frustrate attempts to derive parameterizations that go beyond heuristic or empirical approaches which typically involve tuning of process rates. To make matters

© 2022. The Authors.

This is an open access article under the terms of the [Creative Commons Attribution License](https://creativecommons.org/licenses/by/4.0/), which permits use, distribution and reproduction in any medium, provided the original work is properly cited.

worse, parameterized aerosol and cloud microphysics must be supplemented by parameterizations describing the underlying dynamical forcing, that is, cooling rates induced by the vertical wind field.

Physically-based cirrus formation parameterizations with different degrees of complexity have been developed, starting with the most basic cloud ice nucleation process: homogeneous freezing of aqueous, supercooled solution droplets (Barahona & Nenes, 2008; Dinh et al., 2016; Kärcher & Lohmann, 2002a, 2002b). These schemes have been extended to include INPs forming ice heterogeneously at a sharp ice supersaturation threshold (Barahona & Nenes, 2009a; Kärcher et al., 2006; Kärcher & Lohmann, 2003) and over a broader range of ice supersaturations (Barahona & Nenes, 2009b; Muench & Lohmann, 2020). The Kärcher and Lohmann (2002a) (hereafter K02) and Kärcher et al. (2006) (K06) schemes are employed in a number of numerical weather prediction (NWP) and global climate models (Bock & Burkhardt, 2016; Dietlicher et al., 2019; Hendricks et al., 2011; Köhler & Seifert, 2015; Kuebbeler et al., 2014; Liu & Shi, 2018; Lohmann & Kärcher, 2002; Muench & Lohmann, 2020; Penner et al., 2018; Righi et al., 2020). Some of these schemes are capable of describing ice formation from interstitial aerosols within already-existing cirrus (Shi et al., 2015). Empirical parameterizations for cirrus formation have also been developed and implemented in global models (Gettelman et al., 2010; Liu et al., 2007; Liu & Penner, 2005; Phillips et al., 2008; Salzman et al., 2010).

Competing ice nucleation between solution droplets and INPs in cirrus has recently been studied on the process level with the help of numerical simulations (Kärcher et al., 2022) (hereafter K22), based on substantial progress that has been made in characterizing ice nucleation abilities of INPs (Kanji et al., 2017), mainly in laboratory settings. Progress has also been made in characterizing the magnitude of, and variability in, vertical wind speeds at cirrus altitudes, through quasi-Lagrangian in situ measurements (Podglajen et al., 2016). Moreover, research into the microphysics of ice growth in cirrus conditions gains momentum (Harrington et al., 2019), although uncertainties remain, especially for cold, tropical tropopause layer (TTL) cirrus (K22). The time is ripe to bring all these elements together in an advanced cirrus parameterization scheme.

We seek closure between nucleation spectra of INPs and the resulting ICNCs. In addition, we allow for a competition of heterogeneous ice nucleation with the more basic homogeneous freezing mode. We thereby advance our earlier cirrus formation scheme (K06) that represents heterogeneous ice nucleation crudely as a sharp threshold freezing process. According to experimental evidence, ice-active INP fractions in most cases increase gradually with increasing supersaturation due to the dominant deterministic component of heterogeneous ice nucleation. Thus, the new scheme captures gradual ice activation realistically and in a flexible way, allowing both a measurement-based description of ice activities and a treatment based on idealized ice activation spectra. We also improve the homogeneous freezing scheme (K02 with modifications described in K22). Specifically, the threshold ice supersaturation for homogeneous freezing now also depends on the updraft speed, besides the dependencies on temperature and mean water volume in solution droplets. Furthermore, we abandon the numerical integration of the supersaturation equation in K06 and replace it by solutions that are either fully analytical or involve a simple quadrature.

The foundation and derivation of the new cirrus parameterization is presented in Section 2, which also discusses aspects of its implementation. The scheme is validated and its performance is demonstrated using idealized and real-world INP spectra in Section 3. Effects of pre-existing cirrus ice crystals are discussed in Appendix A and spectra quantifying ice activation of dust and soot INPs are derived in Appendix B. Section 4 summarizes the results of this study.

## 2. Elements of the Parameterization

This section discusses fundamentals of cirrus formation involving INPs and solution droplets, closely following K02 and K22 regarding methodology and notation.

### 2.1. Supersaturation Equation

Central to heterogeneous cloud ice formation is the equation determining the temporal evolution of ice supersaturation,  $s$ , in the ice-vapor system:

$$\dot{s} = \underbrace{a(s+1)w}_{\mathcal{P}} - \underbrace{\int_0^s \frac{4\pi}{\nu n_{\text{sat}}} \frac{dn}{d\sigma} \left( \int_{\tau(\sigma)}^{t(s)} r^2 \dot{r} dt' \right) d\sigma}_{\mathcal{L}} \quad (1)$$

where  $\dot{s}$  denotes the time derivative of  $s$ , the upper integration limit indicates the time  $t$  corresponding to ice supersaturation  $s$ , and the lower limit indicates a time  $\tau$  that corresponds to  $0 \leq \sigma \leq s$ .  $\mathcal{P}$  is the production term (forcing) due to adiabatic cooling,  $\mathcal{L}$  is the loss term (deposition) due to removal of  $\text{H}_2\text{O}$  from the vapor phase,  $r$  is the radius of spherical ice crystals,  $\dot{r}$  is the associated ice crystal growth rate,  $\nu$  is the volume of one  $\text{H}_2\text{O}$  molecule in bulk ice, and  $n_{\text{sat}}$  is the  $\text{H}_2\text{O}$  number concentration in the gas phase at ice saturation. The supersaturation evolution is forced by the vertical wind speed,  $w$ ; here, we restrict ourselves to updraft speeds,  $w > 0$ , taking constant values during the duration of nucleation events. The number concentration of INPs forming ice crystals in a range of supersaturation,  $d\sigma$ , is given by  $dn/d\sigma$ , so that the number concentration of ice crystals cumulated from ice saturation ( $s = 0$ ) up to  $s > 0$ ,  $n(s)$ , follows from

$$n = \int_0^s \frac{dn}{d\sigma} d\sigma, \quad (2)$$

with  $n(s = 0) = 0$ . We explain the use of this time-independent (deterministic) formulation of heterogeneous ice nucleation in Section 2.2, where we also recapitulate the separate treatment of time-dependent (stochastic) homogeneous freezing. The full solution of Equation 1,  $s(t)$ , cannot be derived before  $\dot{r}$  is specified and  $r$  is known (Section 2.3). However, the parameterization is derived without explicit knowledge of  $s(t)$ .

In  $\mathcal{P}$ ,  $a$  is a thermodynamic parameter (Pruppacher & Klett, 1998) determining the rate of change of  $s$  for given  $w$ ,

$$a = \frac{\Gamma}{T} \left( \frac{L}{R_v T} - \frac{c_p}{R} \right), \quad (3)$$

where  $\Gamma = g/c_p$  is the absolute value of the dry adiabatic lapse rate with the acceleration of gravity,  $g$ , and the isobaric specific heat capacity of dry air,  $c_p$ ;  $T$  is the air temperature (ice crystals are assumed to be in thermal equilibrium);  $L$  is the latent heat of sublimation; and  $R$  ( $R_v$ ) is the specific gas constant for air ( $\text{H}_2\text{O}$ ). The variables  $n_{\text{sat}}$  and  $L$  are not independent and a physically self-consistent formulation is used here (Murphy & Koop, 2005).

The forcing term scales in proportion to the updraft speed at the location where ice nucleation events occur. In the atmosphere, the vertical wind field is strongly scale-dependent. Research studies have so far identified the atmospheric mesoscale as crucial in determining values of  $w$  that matter for cirrus formation (Kärcher, 2017a). On the mesoscale, gravity waves induce vertical air motion variability with frequencies limited by buoyancy, leading to adiabatic cooling rates,  $-\Gamma w$ , on the order of  $\text{K h}^{-1}$ . Radiative heating or cooling rates are much smaller ( $\text{K d}^{-1}$ ) and therefore affect supersaturation development only at longer time scales. Radiative cooling or in fact any other large-scale cooling tendencies (e.g., due to synoptic motions) may be converted into an equivalent updraft speed and included in  $\mathcal{P}$  as a constant or slowly varying background, but the effect on ice nucleation in cirrus will be negligible (Kärcher et al., 2019). Radiative and synoptic processes are still important factors controlling the development of for example, tropical cirrus outside convective detrainment zones (Gasparini et al., 2019).

In  $\mathcal{L}$ , latent heat effects due to ice formation and growth are neglected, which is justified due to the low temperatures ( $< 230 \text{ K}$ ) in which most non-convective cirrus form and evolve. The radial growth rate per ice crystal is given by

$$\dot{r} = \frac{b_1 s}{1 + b_2 r}; \quad b_1 = \nu n_{\text{sat}} \frac{\alpha v}{4}, \quad b_2 = \frac{\alpha v}{4 D_v}, \quad (4)$$

with the  $\text{H}_2\text{O}$  diffusion coefficient,  $D_v$ , the mean thermal speed of  $\text{H}_2\text{O}$ ,  $v$ , and the deposition coefficient for uptake of  $\text{H}_2\text{O}$  on the heterogeneously-produced ice crystals,  $\alpha$ . An explicit dependence of  $\dot{r}$  on the air pressure,  $p$  (derived from the adiabatic relationship), arises via  $D_v$ . Defining  $b = b_1/b_2 = \nu n_{\text{sat}} D_v$  is useful in denoting diffusion-limited growth ( $b_2 r \gg 1$ ), where  $\dot{r} = bs/r$ . In the kinetic limit ( $b_2 r \ll 1$ ),  $\dot{r} = b_1 s$ . In the case of ice formation in cirrus, it is important to distinguish diffusion- and kinetically-limited growth regimes (K02). The Kelvin effect reducing the supersaturation is negligible for ice crystal growth owing to the substantial ice supersaturation (tens of per cent) associated with cirrus formation.

Equation 1 is an integro-differential equation that can be integrated numerically. As shown here, specifying  $\mathcal{L}(s)$  and examining the conditions where  $\dot{s} = 0$  is sufficient to estimate total heterogeneously-nucleated ICNCs (limited by the abundance of INPs) for a given forcing (Section 2.3). For later use, we define the quenching velocity,  $w_1$ , according to

$$w_1 \equiv \frac{\mathcal{L}}{a(s+1)}; \quad W = w - w_1, \quad \omega = \frac{w_1}{w}, \quad (5)$$

so that Equation 1 takes the concise form  $\dot{s} = a(s+1)(w - w_1)$ ;  $w_1$  is a measure of the H<sub>2</sub>O sink due to growing ice crystals derived from INPs (K22) or pre-existing cirrus ice crystals (Appendix A). We refer to  $W$  as an effective vertical wind speed and use it in the case  $W > 0$  to estimate the number concentration of homogeneously-produced ice crystals,  $n_{\text{hom}}$ , in the presence of INPs (Section 2.2.1). The nucleation regime (quenching) parameter,  $\omega$ , separates the freezing regime ( $\omega < 1$ ) from the quenching regime ( $\omega > 1$ ). In the freezing regime, INP activation cannot stop  $s$  from rising due to cooling and homogeneous freezing eventually sets in. In the quenching regime ( $\omega > 1$ ), the deposition sink due to heterogeneously-produced ice crystals is strong enough to halt the supersaturation increase and prevent homogeneous freezing. Analogous to homogeneous freezing-relaxation, we refer to the latter situation as ice activation-relaxation.

Three timescales associated with Equation 1 play an important role in evaluating the deposition sink term: the supersaturation relaxation (quenching) time scale,

$$\tau_q = \frac{s}{\mathcal{L}(s)} = \frac{s/(s+1)}{aw_1}; \quad (6)$$

the initial growth timescale,

$$\tau_g = \left( \frac{b_1/r_*}{1 + \delta} \right)^{-1}, \quad \delta = b_2 r_*, \quad (7)$$

where  $r_*$  is the ice crystal radius at the point of nucleation equal to the radius of the (dry) INP core, and the cooling time scale,

$$\tau_c = \frac{1}{aw}, \quad (8)$$

describing the evolution of  $s$  due to cooling ( $w > 0$ ) in the absence of ice crystals. The parameter  $a$  depends weakly on  $T$ ; a typical value at cirrus temperatures is  $10^{-5} \text{ cm}^{-1}$ . Starting at ice saturation, integration of  $\dot{s} = \mathcal{P}$  with constant  $a$  yields

$$s(t) = \exp\left(\frac{t}{\tau_c}\right) - 1; \quad (9)$$

in a constant updraft,  $s$  increases linearly as  $s = awt$  as long as  $t \ll \tau_c$ , a condition that is reasonably well fulfilled in cirrus conditions.

## 2.2. Ice Nucleation Model

### 2.2.1. Homogeneous Freezing

If heterogeneously-produced ice crystals do not induce activation-relaxation,  $s$  continues to increase in a constant updraft despite ongoing depositional growth (i.e., at a slower rate), eventually reaching homogeneous freezing conditions. The stochastic nature of homogeneous droplet freezing requires a modification of the supersaturation loss term in Equation 1. Specifically, the rate of heterogeneous ice activation,  $dn/ds$ , is replaced by a time-dependent freezing rate (with the integration then carried out over time), and estimations of the number concentration of homogeneously-nucleated ice crystals,  $n_{\text{hom}}$ , can be derived as detailed in K02.

Homogeneous freezing events create size-dispersed ice crystals forming at slightly different times. As with INP-derived ice crystals, the competition of homogeneously-produced ice crystals for the available water vapor is taken into account in the corresponding time-integrated supersaturation loss term (Eq. (1b) in K02). Instead

of explicitly adding this term to Equation 1, we follow K22 and estimate the thermodynamic value,  $s_{\text{hom}}$ , where deposition growth of ice crystals originating from already frozen solution droplets quenches the supersaturation by numerical iteration as a function of  $T$ ,  $w$ , as well as the mean size and size spread of the droplet population. We then evaluate the number concentration of additional ice crystals produced homogeneously at  $s_{\text{hom}}$ , using  $W > 0$  in our updated homogeneous freezing parameterization (K02, with modifications described in K22);  $W$  is used instead of  $w$  to take the effect on  $s$  of an evolving deposition sink due to INP-derived or pre-existing cirrus ice crystals into account.

The aqueous aerosol size distribution, either mono- or polydisperse, is an input to the K02 parameterization. In it we use a wet radius of 0.25  $\mu\text{m}$  of monodisperse liquid solution droplets in the present study. While it is key to include INP size information to estimate heterogeneous ice activity, the use of monodisperse spectra for liquid solution droplets allows to predict homogeneously-nucleated ice crystal number concentrations (ICNCs) that are sufficiently accurate in many applications (Ren & MacKenzie, 2005).

The dominating effects of temperature and updraft speed are captured in the homogeneous freezing parameterization via  $s_{\text{hom}}$  (K02 with modifications described in K22), as well as comparatively weaker dependencies on mean solution droplet size and size spread that are relevant in studies of, for example, effects of major volcanic eruptions (Lohmann et al., 2003). However, there is no explicit dependence of homogeneously-nucleated ICNCs on total droplet number concentration,  $n_d$ , in the K02 parameterization, which would likewise induce only a low sensitivity. For example, based on numerical simulations with a detailed parcel model (Kärcher, 2017b) carried out for  $w = 15 \text{ cm s}^{-1}$ ,  $T = 220 \text{ K}$ ,  $p = 250 \text{ hPa}$ , and a baseline value of  $n_d = 500 \text{ cm}^{-3}$  of log-normally distributed solution droplets, we find that halving/doubling  $n_d$  causes ICNC to decrease by 4%/increase by 3%.

The relatively weak dependence of homogeneously-nucleated ICNCs on liquid aerosol properties diminishes in the presence of INPs. Nonetheless, a change of ICNC due to variability in  $n_d$  represents one of the aerosol-related, indirect radiative forcing mechanisms. The large increase in  $n_d$  due to anthropogenic sulfate emissions relative to pre-industrial times can lead to non-negligible global radiative forcing values via cirrus modification (Liu & Shi, 2018). Therefore, studies with an explicit focus on large variations of  $n_d$  preferably include a cirrus parameterization with an explicit  $n_d$ -dependence.

In reality,  $s_{\text{hom}}$  is not a sharp threshold. The maximum ice supersaturation during homogeneous freezing events can increase above  $s_{\text{hom}}$  by a few percent due to overshooting, depending on the magnitude of the updraft speed. The impact on  $n_{\text{hom}}$  is minor in non-convectively generated cirrus, as more significant overshooting requires high updraft speeds ( $> 1 \text{ m s}^{-1}$ ). Nonetheless,  $n_{\text{hom}}$  may be checked by comparison with detailed numerical simulations. Such simulations also include relatively rare non-persistent cooling events (Dinh et al., 2016), where  $W$  changes sign from positive to negative values during freezing; they are not captured by the homogeneous freezing parameterization. These events do not occur frequently in the case of gravity-wave driven variability in vertical wind speeds and may only matter along individual air parcel trajectories on a case-by-case basis (Kärcher et al., 2019), but not in a statistical sense. The latter situation arises, for example, when the parameterization is employed in a large-scale model (Section 2.5.2).

### 2.2.2. Heterogeneous Ice Nucleation

We employ a deterministic (time-independent) approach to predict activation of INPs into ice crystals. For given  $s$ , the associated ICNC is given by

$$n = n_{\text{tot}}\Phi(s), \quad (10)$$

where  $n_{\text{tot}}$  is the total INP number concentration and  $\Phi$  is the ice-active INP fraction (or INP spectrum), cumulated from ice saturation up to  $s > 0$ , obtained from measurements or parameterizations. Whereas  $\Phi$  determines whether an INP is judged as good or poor,  $n_{\text{tot}}$  controls the efficiency of INPs in quenching the supersaturation for given  $w$  via  $\tau_q$  (K22). We emphasize that  $\Phi(s)$  is integrated over the INP size distribution, taking into account the relative abundance of INPs of different size, hence, ice activities. Size distributions and supersaturation spectra for two distinct INP types are presented and discussed in Appendix B.

A deterministic framework is valid for deposition nucleation, because this ice formation mode lacks a liquid water phase to begin with. Immersion freezing is associated with a deterministic and a stochastic component. It is observed that the lower  $T$ , the more ice nucleation sites on the surfaces of immersed INPs become active

and frozen fractions increase. This behavior can either be described by a time-dependent nucleation rate (stochastic approach) or by a distribution of time-independent freezing temperatures (deterministic approach). The latter is applicable, as frozen fractions in a given droplet population typically increase strongly upon cooling, and the associated steep slope is modulated only slightly by a minor stochastic freezing component (Kärcher & Marcolli, 2021). (An additional  $s$ -dependence would arise for immersion freezing in solution droplets in addition to the freezing temperatures.) The pore condensation and freezing (PCF) mode is also described deterministically owing to rapid homogeneous nucleation of ice in liquid water condensed in pores at cirrus temperatures (Marcolli et al., 2021).

In sum, the deterministic approach covers the range of observed ice formation behavior of atmospheric INPs. In this approach, the temperature dependence of heterogeneous ice activation is considered to be more important than the time dependence, in line with a body of experimental evidence. We recall that mesoscale gravity waves produce rapid temperature fluctuations (Hoyle et al., 2005).

To directly compare effects of different functional forms for INP spectra, we also use a formulation equivalent to Equation 10:

$$n = n_* \phi(s), \quad (11)$$

where  $n_* \leq n_{\text{tot}}$  is defined as the INP number concentration determined by the maximum possible ice-active fraction and  $\phi$  is a (size-integrated)  $s$ -cumulated INP spectrum bounded by 0 and 1. For INPs with  $\Phi_{\text{max}} < 1$ ,  $n_* = n_{\text{tot}} \Phi_{\text{max}}$ .

To derive  $\mathcal{L}(s)$  in closed analytical form, we first introduce the Heaviside step function:

$$\phi = \begin{cases} 0 & : s < s_* \\ 1 & : s \geq s_* \end{cases} \quad (12)$$

to describe a population of INPs that activate sharply at  $s_*$  (pulse activation). The differential INP spectrum corresponding to Equation 12 is Dirac's delta function,  $d\phi/ds = \delta(s - s_*)$ . Such INPs do not necessarily correspond to a monodisperse size population, rather INPs from all sizes are required to nucleate ice at the same ice supersaturation. However, even INPs of the same size may activate at different supersaturations due to inter-particle variability. While Equation 12 is therefore clearly an idealization, it proves very useful in describing salient features of the parameterization.

Secondly, we define  $\phi$  more realistically as a linear ramp with an adjustable slope:

$$\phi = \begin{cases} 0 & : s < s_- \\ (s - s_-) / (s_+ - s_-) & : s_- \leq s \leq s_+ \\ 1 & : s > s_+ \end{cases} \quad (13)$$

characterized by two parameters,  $s_-$  and  $s_+$ , denoting zero and full activation, respectively. Alternatively, the two parameters define the range of ice supersaturation where ice activation occurs (slope parameter):  $\Delta s = s_+ - s_-$ , and the 50%-activation level (location parameter):  $s_* = (s_- + s_+)/2$ . Equation 13 thereby captures the two most important parameters controlling ice activity, assuming that activation is symmetric around  $s_*$ ;  $d\phi/ds = 1/\Delta s$  is a top hat distribution that takes zero values outside the range  $[s_-, s_+]$ . Ramp spectra are used to illustrate basic model features (Section 2.3).

Proxies for good and poor INPs have been introduced in K22 based on monodisperse desert dust and aviation soot particles, whose ice activity curves may be approximated by

$$\phi = \frac{1}{2} [\tanh(z) + 1], \quad z = \frac{s - s_*}{\delta s}, \quad (14)$$

with the slope parameter,  $\delta s$ . INP spectra of this form, with  $\delta s = 0.03$ , are also used here for validation (Section 3.1). The derivative of Equation 14 is given by a logistic function,  $d\phi/ds = 2\phi(1 - \phi)/\delta s$ . Hyperbolic tangent spectra are used to compare results from more detailed numerical simulations with the parameterization (Section 3.1).

After careful consideration, Equations 12 and 13 might be used to fit real-world spectra to benefit from the associated fully analytical solutions derived in Section 2.3. This may be relevant to minimize the computational demand of the parameterization in global model applications.

### 2.3. Heterogeneous Ice Activation-Relaxation

To derive a closed expression for  $\mathcal{L}(s)$ , we must know how  $r$ , the radius of ice crystals activating at  $0 < \sigma \leq s$ , depends on the evolving ice supersaturation. To this end, we integrate Equation 4 at constant  $T$  and  $\alpha$ , yielding

$$r(s, \sigma) = \frac{1}{b_2} \left[ (1 + \delta) \sqrt{2 \frac{b_1 b_2}{(1 + \delta)^2} \underbrace{\int_{\tau(\sigma)}^{t(s)} s(t') dt'}_{\mathcal{I}(s)} - 1} \right]. \quad (15)$$

We replace  $\mathcal{I}(s)$  in Equation 15 with the lower-limit estimate derived by Twomey (1959):

$$\mathcal{I}_{\min} = \frac{\tau_c}{2} (s^2 - \sigma^2). \quad (16)$$

and define the scaled radius,  $\rho$ , via

$$\rho(s, \sigma) = b_2 r = (1 + \delta) \sqrt{1 + \kappa (s^2 - \sigma^2)} - 1 \quad (17)$$

together with the growth regime parameter

$$\kappa = \frac{\delta}{1 + \delta} \frac{\tau_c}{\tau_g}, \quad (18)$$

indicating fast ( $\kappa \gg 1$ ) or slow growth ( $\kappa \ll 1$ ) relative to cooling. Faster growth is brought about by higher cirrus temperatures, higher deposition coefficients, and slower updrafts, as  $\kappa \propto \alpha n_{\text{sat}}/w$ .

The initial size parameter,  $\delta$ , typically assumes small values, for example,  $\delta \approx 0.05$  for  $T = 220$  K,  $p = 250$  hPa,  $r_* = 0.25$   $\mu\text{m}$ , and  $\alpha = 0.1$ . Values of  $\kappa$  lie mostly in the fast growth regime, for example,  $\kappa \approx 500$  for these conditions and  $w = 15$   $\text{cm s}^{-1}$ . The fact that vapor deposition on INP-derived ice crystals typically takes place in the fast growth regime is significant and underscores the importance to include activation of INPs into ice crystals across a range of ice supersaturations (K22). Ice crystals from earlier activating INPs quickly grow ahead of those from later activating INPs, thus modifying the supersaturation conditions for later activation.

With Equation 17, the deposition sink then takes the form

$$\mathcal{L} = \frac{4\pi s}{(v n_{\text{sat}})} \frac{b_1}{b_2^2} n_{\text{tot}} \underbrace{\int_0^s \frac{d\Phi}{d\sigma} \frac{\rho^2}{1 + \rho} d\sigma}_{\mathcal{A}(s)}. \quad (19)$$

Note that diffusional limitation to mass transfer from the vapor to ice crystals is reflected by the coefficient  $b_2$  introduced in the ice crystal radial growth Equation 4. If an INP type is represented by Equation 11, then  $n_*$  and  $d\phi/d\sigma$  are used to evaluate  $\mathcal{L}$  replacing  $n_{\text{tot}}$  and  $d\Phi/d\sigma$  in Equation 19, respectively;  $\mathcal{A}(s)$  is the dimensionless activation-growth integral.

The impact of ice activation on  $\mathcal{L}$  grows in proportion to  $\mathcal{A}(s)$ . It also scales linearly with  $n_{\text{tot}}$  ( $n_*$ ) and in a non-linear manner with  $\alpha$ . The scaling of  $\mathcal{L}$  with  $\alpha$  is consistent with the transition from kinetically-limited to diffusion-limited growth. In the prefactor of  $\mathcal{L}$ ,  $b_1/b_2^2 \propto 1/\alpha$ , but the overall  $\alpha$ -dependence of  $\mathcal{L}$  is more complex via  $\delta$  and  $\kappa$ . For  $\delta \ll 1$ ,  $\mathcal{L}$  becomes independent of  $\alpha$  in the fast growth regime—facilitating the use of constant deposition coefficients in the derivation of Equation 15, while in the slow growth regime,  $\mathcal{L} \propto \alpha$ .

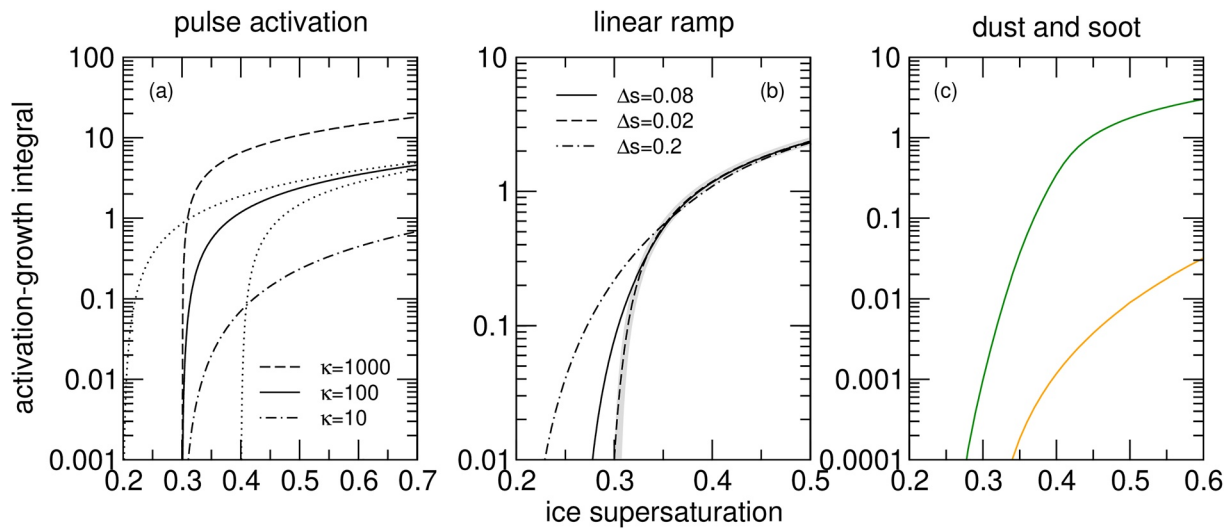


**Figure 1.** Activation-growth integrals versus ice supersaturation (a) for various values of  $\kappa$  in the fast growth regime and instant activation of all INPs at the sharp threshold  $s_* = 0.3$ ; two dotted curves are added for  $s_* = 0.2$  and  $s_* = 0.4$  ( $\kappa = 100$ ). In (b), the result from (a) for  $s_* = 0.3$  and  $\kappa = 100$  is repeated as a gray curve and results from the linear ramp with various widths  $\Delta s$  are added. In (c), results for (green) desert dust and (orange) contrail-processed aviation soot from the original parameterizations (for both INP types,  $\kappa = 100$ ). All curves assume  $\delta = 0$ .

For pulse activation, Equation 12,  $\mathcal{A}$  is given by

$$\mathcal{A}(s \geq s_*) = \frac{\rho^2(s, s_*)}{1 + \rho(s, s_*)}, \quad (20)$$

and  $\mathcal{A}(s < s_*) = 0$ . Equation 20 serves as the fundamental solution, meaning that any other solution must show the same asymptotic scaling above  $s_*$ .

For the linear ramp, Equation 13,  $\mathcal{A} = 0$  below the activation region ( $s < s_-$ ). Within and above the activation region,  $\mathcal{A}$  is calculated to be

$$\mathcal{A}(s \geq s_-) = \frac{1}{\Delta s} \left[ \frac{1 + \delta}{2} s \{ (1 + \kappa s^2) [f(z_+) - f(z_-)] + [g(z_+) - g(z_-)] \} + \frac{1}{1 + \delta} s \{ f(z_+) - f(z_-) \} \right] - 2\Phi(s), \quad (21)$$

with  $z_- = s_-/s \leq 1$  and the auxiliary functions

$$f(z) = \frac{1}{s\sqrt{\kappa}} \arcsin \left( z \cdot \sqrt{\frac{\kappa s^2}{1 + \kappa s^2}} \right) \quad (22)$$

and

$$g(z) = z \cdot \sqrt{1 + \kappa s^2 (1 - z^2)} \quad ; \quad (23)$$

note that within the interval  $[s_-, s_+]$ ,  $z_+ = 1$ , but for  $s > s_+$ ,  $z_+ = s_+/s < 1$ .

For INP spectra  $\Phi(s)$  that are not available analytically or for Equation 14,  $\mathcal{A}$  follows from numerical integration. In all cases, the solution is generalized to  $J$  INP types, each with constant deposition coefficients,  $\alpha_j$ , by

$$\mathcal{L} \rightarrow \sum_{j=1}^J \mathcal{L}_j = \frac{4\pi s}{(vn_{\text{sat}})} \sum_{j=1}^J \frac{b_{1j}}{b_{2j}^2} n_{\text{tot},j} \mathcal{A}_j(s). \quad (24)$$

We evaluate  $\mathcal{A}(s)$  for different INP spectra and a single INP type ( $J = 1$ ) following Equation 11 and show the results in Figure 1. As justified above, we set  $\delta = 0$  and only show solutions in the fast growth regime ( $\kappa \gg 1$ ).

Figure 1a shows that for pulse activation at the sharp threshold  $s_*$ , no INPs activate below  $s_*$  by design. Above  $s_*$ ,  $\mathcal{A}$  increases sharply as ice crystals begin to deposit  $\text{H}_2\text{O}$ . Moreover,  $\mathcal{A}$  increases (decreases) with  $\kappa$  due to

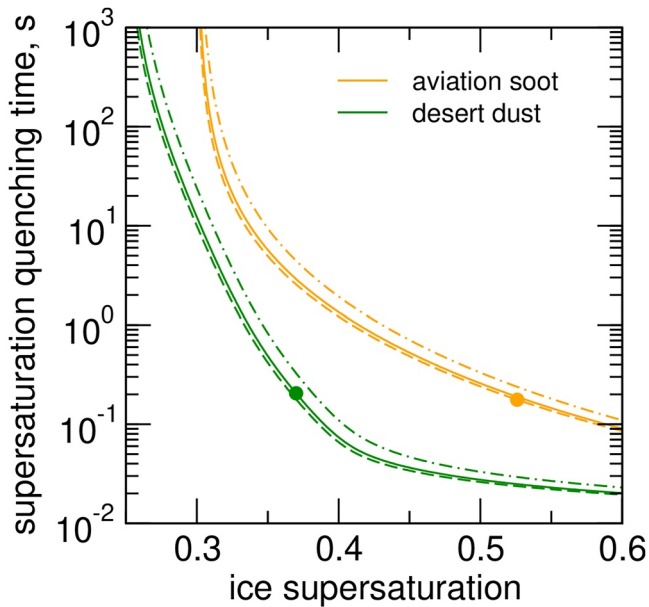


**Figure 2.** Supersaturation quenching times for desert dust and contrail-processed aviation soot evaluated at typical upper tropospheric conditions at northern midlatitudes versus ice supersaturation. The dot-dashed (solid, dashed) curves assume  $\alpha = 0.1$  (0.3, 0.7) for each INP type. Circles mark conditions where the ice activities of desert dust and contrail-processed aviation soot maximize below and alongside homogeneous freezing, respectively.

larger (smaller) growth rates. Better (poorer) INPs activate at a lower (higher) supersaturation threshold and therefore begin to deplete the vapor earlier (later), leading to a higher (lower) value of  $\mathcal{A}$  before the asymptotic scaling is reached (e.g., around  $s = 0.7$  for  $\kappa = 100$ ). Importantly, a deposition sink reduced by growth on INP-derived ice crystals in the freezing regime eventually leads to a decrease in homogeneously-produced ICNCs that is more pronounced the lower  $s_*$ . All these observations are consistent with numerical simulations (K22).

The solution for pulse activation at  $s_* = 0.3$  is repeated for  $\kappa = 100$  in Figure 1b and shown together with ramp solutions for three different widths in which ice activation occurs symmetrically around  $s_* = 0.3$ . The narrowest ramp with  $\Delta s = 0.02$  practically coincides with pulse activation, while the results obtained with larger widths show increased vapor uptake already at  $s < s_*$ . The curves with  $\Delta s = 0.02$  and  $0.08$  converge around  $s = 0.35$ , that is, slightly above  $s_*$ . In the case of a very broad activation region ( $\Delta s = 0.2$ ), the last ice crystals form at  $s = 0.4$  resulting in a slight difference to the pulse activation solution up to even higher  $s$ -values.

Results for desert dust and aircraft-emitted soot particles processed in contrails are presented in Figure 1c based on the nucleation spectra derived in Appendix B. While  $\kappa$ -values may differ for different INPs (e.g., due to different  $\alpha$ , see Section 3.1), we set  $\kappa = 100$  for both INP types along with  $\delta = 0$ . The dust spectrum represents background conditions at cirrus levels in the northern hemisphere. The soot spectrum represents an upper-limit (in terms of mean diameter and size spread) and thus maximizes the particle's ice activity. Nonetheless, the aircraft-emitted and contrail-processed soot particles are much poorer INPs than dust due to a significantly smaller magnitude of  $\mathcal{A}$  across all supersaturations, consistent with the corresponding spectra (Figure B1).

Heterogeneous ice activation-relaxation halts the increase of ice supersaturation ( $\dot{s} = 0$ ) due to adiabatic cooling and therefore occurs when the condition  $\mathcal{P} = \mathcal{L}$  (equivalent to  $w = w_i$ ) is met. The corresponding solution,  $0 < \hat{s} \leq s_{\text{hom}}$ , is determined by numerical iteration using Equation 24. On the one hand, the use of Equation 16 underestimates  $\mathcal{L}$ , which in turn overestimates  $\hat{s}$ . On the other hand, we derive the solution with constant  $T$ , which underestimates  $\hat{s}$ . These effects tend to offset each other.

#### 2.4. Ice Supersaturation Quenching Times

We illustrate supersaturation quenching times from Equation 6 describing the relaxation of  $s$  toward ice saturation due to depositional growth of ice crystals derived from desert dust and aviation soot INPs in Figure 2. To this end, we evaluate Equation 19 for midlatitude cirrus conditions,  $T = 220$  K,  $p = 250$  hPa,  $w = 15$  cm s<sup>-1</sup>, and  $n_{\text{tot}} = 500$  L<sup>-1</sup> for soot ( $n_{\text{tot}} = 28$  L<sup>-1</sup> for dust). The discussion of INP spectra in Appendix B reveals that practically all dust particles become ice-active above about  $s = 0.4$  and that only about 1% of the soot particles are actually ice-active at  $s \approx 0.5$ . Differences in deposition coefficients to be used in the parameterization exist between dust and soot. As  $\alpha$  depends on  $s$ , we evaluate  $\tau_q(s)$  for various  $\alpha$ -values.

For given  $s$ , the soot INPs with lower ice activity and higher ice activation thresholds are associated with longer quenching times than the dust INPs, as  $\tau_q$  mirrors the inverse of the activation-growth integrals shown in Figure 1 according to Equation 6. For both INP types, quenching times get rather long ( $>100$  s) for low supersaturations approaching their size-integrated ice activity thresholds (Figure B1). They increase with decreasing  $s$  as ice growth rates slow down and decrease with increasing total ice-active INP number concentrations enhancing deposition losses. Figure 2 also shows that the dependence of  $\tau_q$  on  $\alpha$  is weak as long as  $\alpha > 0.1$ , implying that  $\tau_q$  is more strongly affected by differences in ice-active INP numbers. Longer quenching times are generally brought about by decreasing  $T$  due to slower growth rates via  $n_{\text{sat}}$  and by increasing  $w$  as the ice-vapor system is pushed toward the slow growth regime, see Equation 18.

The cooling time scale corresponding to the chosen updraft speed and temperature is according to Equation 8  $\tau_c \approx 6, 700$  s and the timescale of an homogeneous freezing event is about 60 s (Kärcher & Jensen, 2017). Comparing these time scales with  $\tau_q$  reveals further insights. In the case of dust, this leads to  $\tau_q \approx 0.2$  s, meaning that dust INPs present in background concentrations have a strong potential to prevent homogeneous freezing. A similar quenching time is predicted for aviation soot, but only at a much higher supersaturation indicating that even this poor INP type may be capable of modifying homogeneous freezing events to a degree when present in sufficiently high number concentrations; this is indeed predicted by a comprehensive cirrus model (Kärcher et al., 2021) and replicated by the parameterization (Section 3.1).

## 2.5. Implementation

### 2.5.1. Parameterization

Figure 3 illustrates the workflow of the new parameterization scheme when implemented in a host model, for example, an NWP or climate model. Input parameters (gray box) comprise meteorological conditions ( $w, T, p$ ), parameters characterizing properties of multiple INPs ( $n_{\text{tot}}, \Phi_j(s)$ ), and the deposition coefficients ( $\alpha_j$ ) affecting the growth rate of ice crystals derived from them and, hence, their ability to perturb or prevent homogeneous freezing.

In a first step, the maximum possible ice supersaturation,  $s_{\text{hom}}$ , is determined as if no INPs and no pre-existing ice crystals were present ( $w_i = 0$ ) and the solution  $n_{\text{hom}}$  is calculated at the input updraft speed employing the homogeneous freezing parameterization (orange box). Otherwise,  $w_i$  is evaluated at the homogeneous freezing threshold,  $s_{\text{hom}}$ , summed over all INP types plus cirrus ice crystals (if present). In the freezing regime ( $\omega = w_i/w < 1$ ),  $n_{\text{hom}}$  is evaluated at the effective updraft speed ( $W = w - w_i > 0$ ) and  $n$  is estimated at  $s_{\text{hom}}$ . Their sum is the total nucleated ICNC (blue box). In the quenching regime ( $\omega > 1$ ),  $s_{\text{hom}}$  is never reached due to activation-relaxation and the value  $\hat{s} < s_{\text{hom}}$  is determined iteratively. The total nucleated ICNC is then given by the cumulative number concentration of INPs that are ice-active at  $\hat{s}$  (green box). We recall that  $s_{\text{hom}}$  is evaluated at  $T, w$ , and (not listed in Figure 3) the mean size and standard deviation of a log-normal solution droplet population (Section 2.2.1).

If ice activation for type- $j$  INPs follows a linear ramp or the hyperbolic tangent, the spectrum,  $\phi_j(s)$ , is fully described by  $s_{-j}$  and  $s_{+j}$  or  $s_{*j}$  and  $\delta s_j$ , respectively. The dependence of heterogeneously nucleated ICNCs on  $r_*$  is small for typical values up to a few 100 nm, since initial growth takes place in the fast growth regime (Section 2.3). For simplicity and without loss of accuracy, we set  $r_*$  equal to 0.2  $\mu\text{m}$  and use the same value for all INP types without formally counting  $r_*$  as an input parameter. If new ice formation takes place within already-existing cirrus, three further input parameters are necessary (Appendix A).

Although deposition coefficients vary with ice crystal size and ambient conditions due to the surface kinetic resistance to vapor growth, the parameterization in its present form uses constant values for each INP type, as supersaturation and other parameters generally vary differently across INP types during nucleation and subsequent deposition growth (K22). K22 pointed out that ice growth from the vapor needs further study. On the one hand, it is currently unclear if deposition coefficients predicted by the step nucleation model for faceted ice growth employed by K22 apply to freshly nucleated ice crystals, especially for low ice supersaturations and in the case of TTL cirrus. On the other hand, competing ice nucleation unfolds at high ice supersaturation (typically  $>0.3$ ), where uncertainties in current models for  $\alpha$  are less problematic as growth is more frequently diffusion-limited and formulations with constant  $\alpha$ -values seem feasible.

The numerical iterations required to determine  $s_{\text{hom}}$  and  $\hat{s}$  are unproblematic so that the final solutions, nucleated ICNCs, are obtained with very little computational effort for an arbitrary number of INP types and pre-existing cirrus ice crystals. Additionally, a quadrature is required to solve the activation integral if the associated INP spectrum does not conform to the linear ramp or pulse approximation. Taken together, the scheme works with a minimal set of physical input parameters, is flexible in terms of INP spectra, does not involve tuning, and is numerically stable and computationally efficient. The parameterization is formulated for one value of  $w$  on input. It may be called multiple times for a distribution of  $w$ -values and its results may be averaged (Section 3.2.2).

### 2.5.2. Host Model

Providing INP-related parameters and updraft speeds as input to the cirrus parameterization requires the use of respective submodels within the host model calling the parameterization.

Total INP number concentrations ( $n_{\text{tot}}$ ), surface coatings and mixing states (affecting ice activity) may change over time as a result of transport, emission, scavenging, and removal processes, as simulated in the host model. For

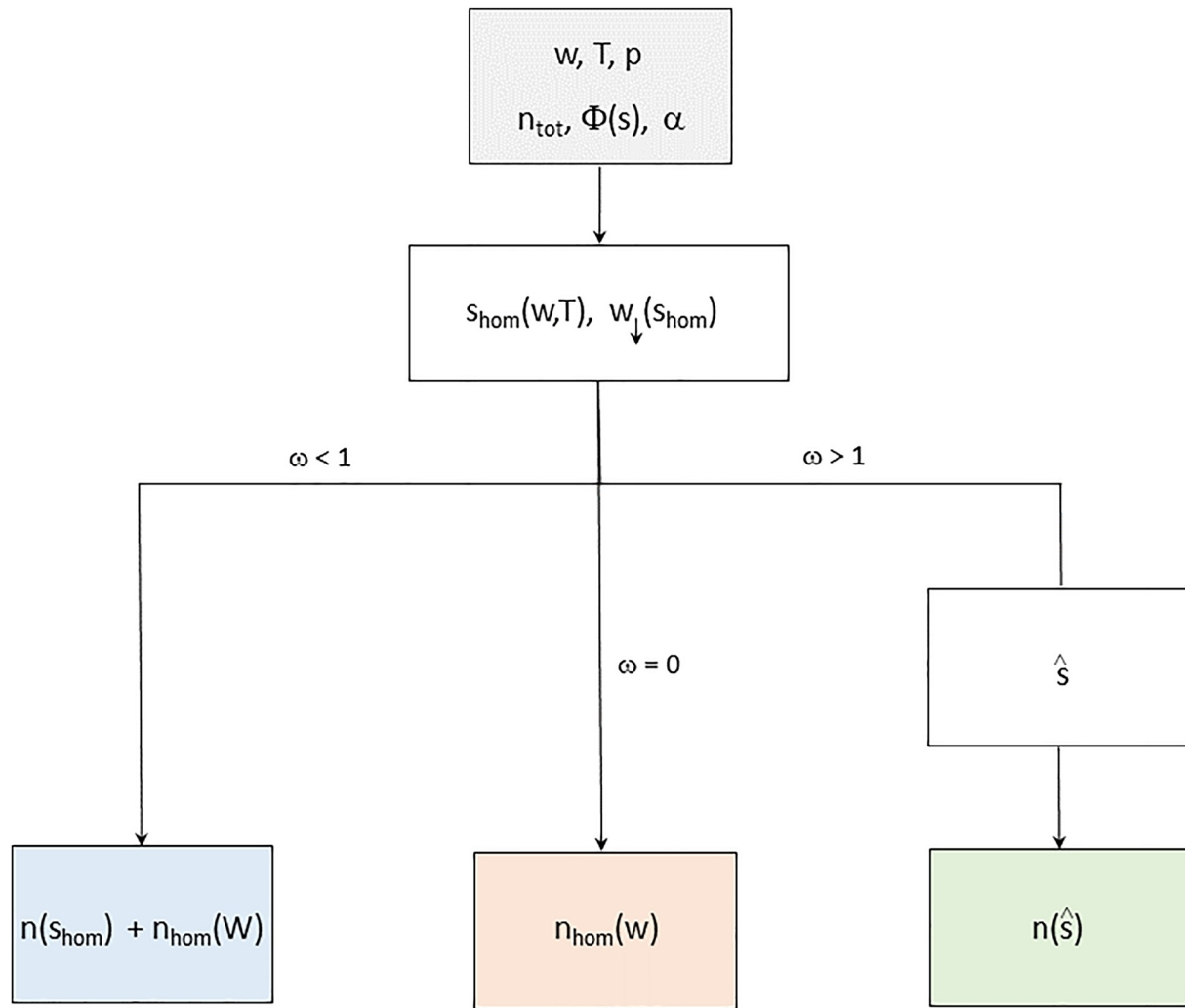


**Figure 3.** Algorithmic representation of the cirrus parameterization scheme describing competing ice nucleation involving one INP type and solution droplets in clear-sky conditions. Input parameters provided by a host model are given in the top box. The homogeneous freezing-relaxation threshold,  $s_{\text{hom}}$ , is determined. If no INPs are present ( $\omega = 0$ ), the ICNC due to homogeneous freezing,  $n_{\text{hom}}$ , is evaluated at the updraft speed,  $w$ , by means of a separate parameterization (K02, K22). Otherwise, the quenching velocity,  $w_1$ , is evaluated at  $s_{\text{hom}}$ , leading to  $\omega > 0$ . In the freezing regime ( $\omega < 1$ ), the ICNC derived from INPs are evaluated at  $s_{\text{hom}}$  based on an ice activation model and  $n_{\text{hom}}$  is evaluated at the effective updraft speed,  $W$ , to account for the presence of INPs. In the quenching regime ( $\omega > 1$ ), homogeneous freezing conditions are not met. The heterogeneous ice activation-relaxation threshold,  $\hat{s}$ , and the corresponding ICNC,  $n(\hat{s})$ , are determined. The bottom boxes indicate the output in each case.

instance, to account for reduction of  $n_{\text{tot}}$  due to INP activation, the calculation of ice activation must be based on differential instead of  $s$ -cumulative ice-active fractions, as INPs need to be budgeted (Kärcher & Marcolli, 2021; Tully et al., 2022). Chemical processes such as the formation of aqueous coatings on INP surfaces may alter the  $s$ -dependence of ice-active fractions. In such cases, the parameters describing the ice activity of INPs must therefore be updated before a new call of the parameterization.

High-resolution NWP models, let alone global climate models, underestimate the variability in vertical wind speed variance due to gravity waves, as shown by a comparison of observed intrinsic frequency spectra of associated Lagrangian fluctuations to model spectra (Podglajen et al., 2020). To accommodate effects of variability in  $w$  unresolved in the host model, the missing variance must be parameterized as a function of time and location. We refer to Kärcher and Podglajen (2019) for further discussion.

There are two ways to obtain a statistically representative set of nucleated ICNCs and thereby the mean ICNC value to be used by the host model depending on its spatial resolution, once a distribution describing the frequency of occurrence of updraft speeds due to mesoscale gravity waves is formulated. The parameterization may be

called at a sufficiently large number of  $w$ -values drawn from the distribution, corresponding to individual air parcel trajectories within a grid box of the host model with distinct temporal evolutions of  $w$  around the same mean value. Alternatively, either the mean updraft speed or one trajectory selected randomly from the distribution may be used to evaluate the nucleated ICNC.

When applying the parameterization in models with time steps smaller than  $\tau_q$  (Figure 2), nucleation is split over several time steps (Köhler & Seifert, 2015), in which case ice crystals that already formed on INPs need to be treated formally as pre-existing ice. In global models, where this issue is less critical due to longer time steps, it may be necessary to check whether nucleation conditions are reached within the time step in the first place, depending on the initial value of  $s$  in the grid box.

Due to the coarse spatial resolution of most global models, it is not known whether cirrus formation takes place in the cloud free or in the cloudy part of a grid box. The cloud fraction variable distinguishes between these cases. A grid box-average value for the nucleated ICNC can be estimated from two calls to the parameterization, delivering results for cloud-free and cloudy conditions, that may be weighted by the cloud fraction.

### 3. Results and Discussion

#### 3.1. Performance and Validation

##### 3.1.1. Comparison With a 1D Cirrus Model

Detailed simulations of contrail-processed soot particles emitted by aircraft at cruise competing with solution droplets in cirrus formation have been reported by Kärcher et al. (2021) based on a comprehensive one-dimensional cirrus model. We use results from their background scenario to directly validate our parameterization scheme. We prescribe  $T = 220$  K,  $p = 250$  hPa,  $n_{\text{tot}} = 500$  L<sup>-1</sup>, and  $w = 15$  cm s<sup>-1</sup> and use the same INP spectrum (Figure B1) as the cloud model.

Soot-derived ice crystals form at high ice supersaturation alongside homogeneous freezing, that is, close to  $s_{\text{hom}}$  where  $\alpha \rightarrow 1$ . The homogeneous freezing parameterization yields  $s_{\text{hom}} = 0.526$ , slightly above the value in the cloud simulation. As soon as the ice crystals grow and begin to settle out of the homogeneous freezing layer, associated  $\alpha$ -values decrease in the cloud model. We therefore make the plausible choice  $\alpha = 0.7$ , supported by laboratory measurements (Skrotzki et al., 2013), a suitable average across the simulated values associated with the soot-derived ice crystals at the time where competition with homogeneous freezing takes place. This choice overestimates the impact of soot INPs activating before homogeneous freezing sets in and thereby forming ice crystals with associated lower  $\alpha$ -values, but the impact is small owing to very low number concentrations of early activating soot particles and the rather weak dependence of  $\tau_q$  on  $\alpha > 0.1$  (Figure 2).

The parameterization predicts  $w_1(s_{\text{hom}}) \simeq 3$  cm s<sup>-1</sup>, so that homogeneous freezing is not prevented, but homogeneously-produced ICNCs are reduced by about 30%, similar to the reduction in simulated column-averaged values. Repeating the comparison at  $w = 1$  cm s<sup>-1</sup>, we find that homogeneous freezing is suppressed ( $w_1(s_{\text{hom}}) \simeq 11$  cm s<sup>-1</sup>), again in agreement with the cloud simulations. The soot INPs reduce homogeneously-nucleated ICNCs in the cloud model despite their low ice-active number concentrations, because the associated deposition coefficients are high near the point of maximum activation (close to  $s_{\text{hom}}$ ), the freshly nucleated ice crystals grow quickly, and the associated supersaturation quenching time (Figure 2) is sufficiently short.

We judge this agreement as satisfactory inasmuch as a fair comparison between the parameterization and the column model is possible. Contrary to the parameterization, the cirrus model accounted for ice crystal sedimentation and used altitude-dependent temperature and moisture fields as well as  $s$ -dependent deposition coefficients. Moreover, highly supersaturated air was slowly entrained into the cloud column. For this reason, the homogeneous freezing parameterization predicts a lower baseline ICNC (unperturbed by soot), hence, we only compare the reduction due to soot in relative terms.

##### 3.1.2. Comparison With Parcel Model Simulations

The process-oriented model described in K22 is well suited to check the performance of the parameterization. The processes underlying Equation 1 are formulated in a parcel model framework with basically identical microphysical equations for spherical ice crystals. INP activation is simulated by dividing INP spectra into

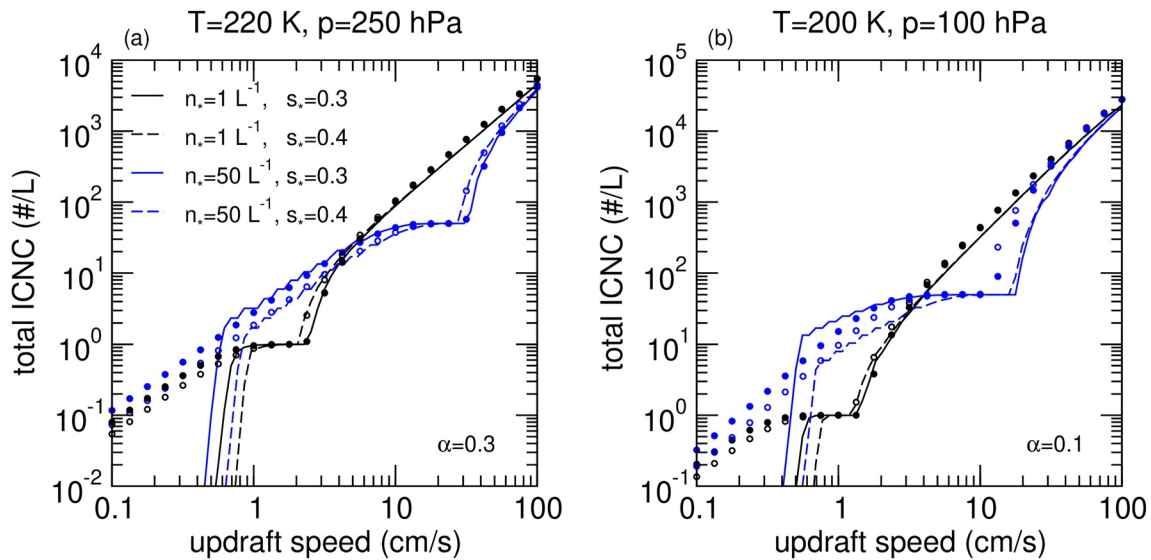


**Figure 4.** Total nucleated ice crystal number concentration versus updraft speed for (a) midlatitude and (b) TTL cirrus. Results from (curves) numerical simulations for INPs with different ice-active number concentrations,  $n_*$ , and location parameters,  $s_*$ , following a hyperbolic tangent activation spectrum are compared with (circles) results from the parameterization. The latter uses fixed deposition coefficients,  $\alpha$ . The sharp decline of ICNC at low updraft speeds is an artifact in the numerical simulations (see text); the parameterization correctly returns values constrained by the total INP number concentration and activation spectrum.

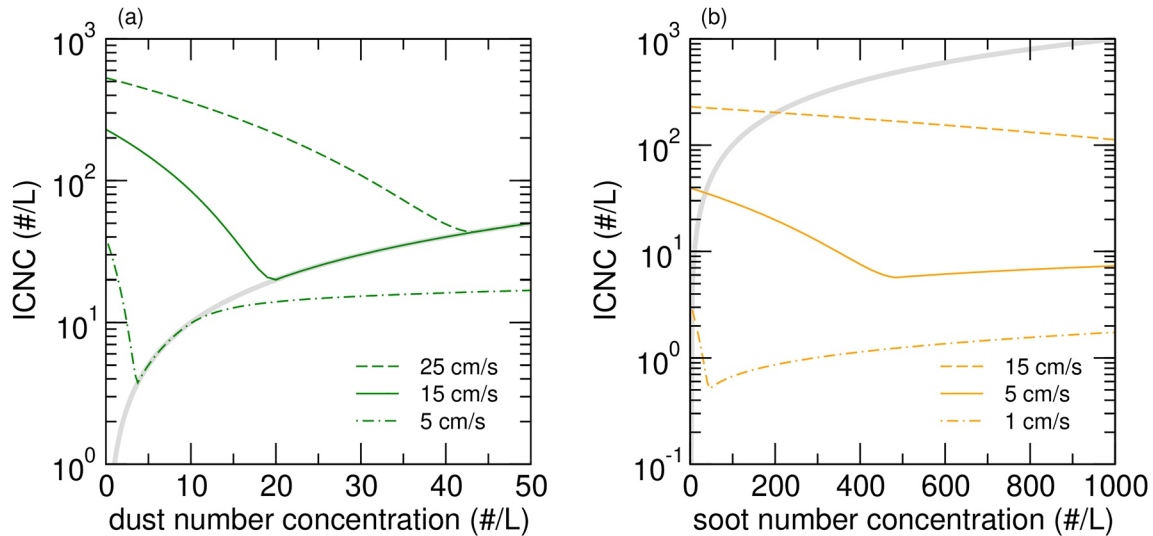
discrete ice supersaturation classes. The main difference is that the numerical simulations account for the proper time-dependence of  $T$  and other variables (due to prescribed vertical wind speeds), solves the deposition loss term without approximation using variable  $\alpha$  based on a simplified ice crystal growth model, and — in the case of forcing due to gravity waves — uses stochastic time series of vertical wind speed fluctuations.

Figure 4 compares total nucleated ICNCs from both approaches for a wide range of constant updraft speeds. As in the simulations, the INP spectrum in the parameterization is defined according to Equation 14 with  $\delta s = 0.03$ . Two sets of simulations with either low ( $n_* = 1 \text{ L}^{-1}$ ) or high ( $50 \text{ L}^{-1}$ ) INP number concentration and location parameter  $s_* = 0.3$  or  $0.4$  are compared. Recall that the ice-nucleation ability of such INPs is comparable to desert dust (Appendix B).

We first discuss the midlatitude cirrus case (220 K, 250 hPa) and fix  $\alpha = 0.3$  in the parameterization. In all four cases, the agreement with the simulation results is excellent for most  $w$  (Figure 4a). Only for the lowest updraft speeds ( $<0.5\text{--}0.8 \text{ cm s}^{-1}$ ), the parameterization (correctly) predicts larger ICNCs. This is due to an artifact of the numerical simulations, because the time it takes to reach nucleation conditions in sufficiently weak updrafts gets longer than the prescribed total simulation time so that the cloud model stops before activation occurs, returning zero ICNCs. Pure homogeneous freezing conditions are approached for updraft speeds  $>10 \text{ cm s}^{-1}$  ( $n_* = 1 \text{ L}^{-1}$ ) and for  $>100 \text{ cm s}^{-1}$  ( $n_* = 50 \text{ L}^{-1}$ ). Especially for high ice-active INP number concentrations, the plateau regions of near constant ICNC (approaching or equal to  $n_*$ ) before homogeneous freezing sets in broaden significantly, confirming that INPs have a marked ability to compete with homogeneous freezing.

Deposition coefficients are large ( $>0.5$ ) as  $s$  approaches  $s_{\text{hom}}$  and  $\alpha$  decreases with increasing ice crystal size (K22). Most of the vapor is consumed by the INP-derived ice crystals in the range  $[s_*, s_{\text{hom}}]$ . When  $s$  falls below a critical value in the relaxation stage ( $s_{\text{crit}}$ , a characteristic of the molecular ice growth model underlying the numerical simulations),  $\alpha$  declines rapidly to values  $<0.1$ . For 220 K,  $s_{\text{crit}} = 0.19$ ; the value  $\alpha = 0.3$  is therefore meaningful. Constant deposition coefficients that best reproduce the temporal evolution of the deposition sink term depend on  $w$  and  $T$  (K22), so that a better agreement in Figure 4a may be obtained by prescribing constant but  $w$ -dependent  $\alpha$ -values in different cirrus temperature regimes.

For cirrus simulated under conditions prevailing in the TTL (200 K, 100 hPa), a value  $\alpha = 0.1$  is used. This value is lower due to a significantly higher  $s_{\text{crit}}$ -value (0.36) in the ice growth model, implying that simulated  $\alpha$ -values of INP-derived ice crystals are on average lower. The tendency of competing nucleation in cold cirrus to produce larger ICNCs is well captured by the parameterization (Figure 4b), but the overall agreement with the



**Figure 5.** Total nucleated ice crystal number concentration versus total number concentration of (a) desert dust particles and (b) contrail-processed aviation soot particles taken from the parameterization for various fixed updraft speeds. The gray curve in each panel indicates the 1:1 relationship.

simulation results is somewhat poorer than in the case of midlatitude cirrus. For instance, in the  $n_{\star} = 50 \text{ L}^{-1}$ -case the parameterization predicts an onset of homogeneous freezing within 10–20  $\text{cm s}^{-1}$  earlier than the numerical model indicates.

We recall the note of caution regarding current models of  $\alpha$  (Section 2.5.1). While the results shown in Figure 4 demonstrate the strong capability of the parameterization to replicate results of numerical simulations with variable  $\alpha$ , quantitative results may be subject to change until ice growth models are better understood, affecting the proper choice of constant  $\alpha$ -values for INPs in the parameterization. This holds especially true for TTL cirrus due to high  $s_{\text{crit}}$ -values and the potential modification of the ice saturation vapor pressure (Section 2.1).

### 3.2. Competing Nucleation

#### 3.2.1. Reduction of Homogeneous Ice Crystal Numbers

Competing processes in ice nucleation are further analyzed with the help of Figure 5, where the effect of dust and soot particles on total nucleated ICNCs for selected updraft speeds is shown. The parameters for midlatitude cirrus are the same as in the discussion of supersaturation quenching times (Section 2.4), using  $\alpha = 0.3$  (0.7) for dust (soot). In the absence of INPs,  $n_{\text{tot}} = 0$ , the results show how homogeneously-nucleated ICNCs vary with  $w$ . With increasing  $n_{\text{tot}}$ , these values diminish significantly and in characteristic ways.

We first discuss the dust case in Figure 5a. Due to the presence of dust particles, total ICNCs decrease with increasing  $n_{\text{tot}}$  to values of about  $4 \text{ L}^{-1}$  ( $w = 5 \text{ cm s}^{-1}$ ),  $20 \text{ L}^{-1}$  ( $15 \text{ cm s}^{-1}$ ), and  $43 \text{ L}^{-1}$  ( $25 \text{ cm s}^{-1}$ ). Up to these concentration values, the dust INPs do not prevent homogeneous freezing, but their effect weakens as  $w$  increases because associated deposition losses are less and less capable of balancing the increasing cooling tendency. For higher  $n_{\text{tot}}$ -values, ice crystal and dust numbers are identical, indicating full activation except in the weakest updraft ( $5 \text{ cm s}^{-1}$ ), where only a fraction of the dust particles form ice when present in concentrations exceeding  $\approx 10 \text{ L}^{-1}$ . Consequently, at  $n_{\text{tot}} = 28 \text{ L}^{-1}$ , ice supersaturation where activation-relaxation or freezing-relaxation occurs amounts to  $\hat{s} = 0.38$  ( $5 \text{ cm s}^{-1}$ ),  $\hat{s} = 0.47$  ( $15 \text{ cm s}^{-1}$ ), and  $\hat{s} = 0.527$  ( $25 \text{ cm s}^{-1}$ ); only in the latter case, homogeneous freezing is activated and will be suppressed for  $n_{\text{tot}} > 42 \text{ L}^{-1}$ .

In the same way, increasing soot particle number concentrations initially lowers homogeneously-nucleated ICNCs (Figure 5b). However, contrary to dust, none of the ICNC curves equal the total soot concentrations, because only a small fraction of the soot particles becomes ice-active. Again, this fraction increases with  $w$ , as faster updrafts cause ice supersaturation to peak at higher values, hence, greater ice activity. In detail,  $\hat{s} = 0.387$  and  $\Phi_{\text{max}} = 0.0025$  ( $1 \text{ cm s}^{-1}$ ),  $\hat{s} = 0.521$  and  $\Phi_{\text{max}} = 0.011$  ( $5 \text{ cm s}^{-1}$ ), and  $\hat{s} = 0.526$  and  $\Phi_{\text{max}} = 0.012$  ( $15 \text{ cm s}^{-1}$ ).

Based on these results, it is safe to conclude that in situations where both dust and soot particles compete with homogeneous freezing, soot particles lead to an additional reduction of homogeneous ice crystal numbers only at

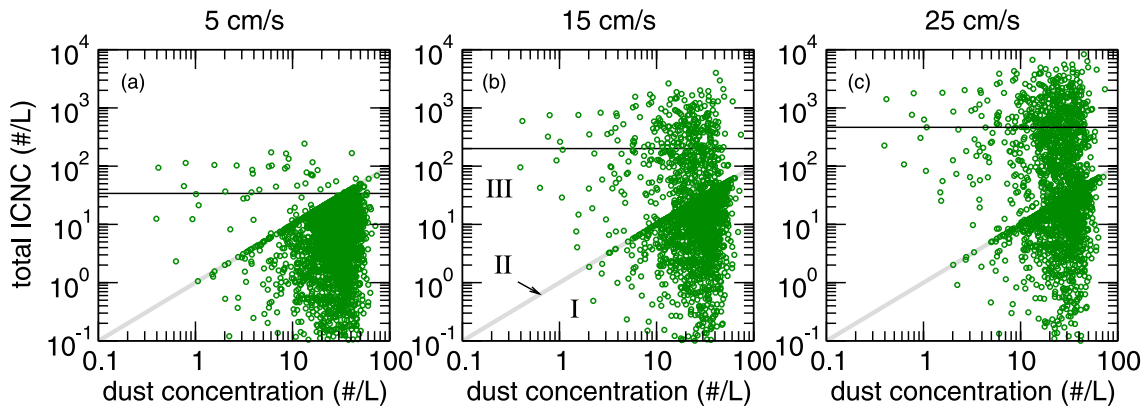


**Figure 6.** Total nucleated ice crystal number concentration versus total number concentration of desert dust particles. To drive the parameterization, updraft speeds are distributed exponentially with standard deviations as indicated above each panel. In each case, dust concentrations are normally distributed with a mean  $28 \text{ L}^{-1}$  and standard deviation  $12 \text{ L}^{-1}$ . Gray lines indicate the 1:1 relationship. Each panel shows 2, 500 individual data points. Region I: partial activation of dust; region II: full dust activation suppressing homogeneous freezing; region III: homogeneous freezing occurs despite full dust activation. Vertical black lines mark mean ICNCs due to pure homogeneous freezing.

low dust number concentrations (depending on  $w$ ), because only then homogeneous freezing is not prevented by dust. We recall that this applies to dust INP that behave like desert dust and contrail-processed, aircraft-emitted soot particles.

### 3.2.2. Ensemble Statistics of Nucleated ICNCs

The effect of updraft speed variability on cirrus formation is captured in ensemble simulations (Section 2.5.2). To this end, we sample updraft speeds from a double-sided exponential function (Laplacian) to model the frequency of occurrence of vertical wind speed fluctuations due to mesoscale gravity waves (Podglajen et al., 2016) and drive the cirrus parameterization. The Laplacian is fully characterized by the fluctuation standard deviation,  $\sigma_w$ . This is different from numerical simulations (K22), where  $w(t)$  is held constant within an autocorrelation time (2.8 min in the upper troposphere) before a new value is sampled from the Laplacian. In a statistical sense, mean ICNCs from both approaches should be equivalent (Kärcher et al., 2019).

To include variability in INP number concentrations consistent with background conditions in the northern hemisphere upper troposphere for dust (Appendix B), we prescribe a Gaussian frequency distribution centered at  $28 \text{ L}^{-1}$  with a standard deviation of  $12 \text{ L}^{-1}$ . Other parameters are chosen as in the last section, so that the results can be directly compared with those shown in Figure 5b that were obtained using single updraft speeds.

Each panel in Figure 6 allows us to divide the data points into three main categories. In category I, updraft speeds are low enough to only partially activate the dust particles inducing activation-relaxation, so that ICNCs are smaller than the total dust number concentrations,  $n < n_{\text{tot}}$ . In category II, all dust particles activate into ice crystals,  $n = n_{\text{tot}}$ , and their total numbers are high enough to prevent homogeneous freezing across a range of higher updraft speeds. Therefore, in cat I and cat II,  $\hat{s} < s_{\text{hom}}$ . The cat II data points on the 1:1 line correspond to those lying in the plateau regions shown in Figure 4; their deposition growth prevents homogeneous freezing from occurring. In cat III, updraft speeds are high enough to allow homogeneous freezing ( $\hat{s} = s_{\text{hom}}$ ) despite full activation of the dust particles,  $n > n_{\text{tot}}$ , and the dust INPs cause a reduction in homogeneously-nucleated ICNCs (compared to cases without dust).

For comparison, we calculate ICNCs for pure homogeneous freezing with the same  $w$ -variability statistic. For the three cases shown in Figure 6, we obtain  $n_{\text{hom}} = 34 \text{ L}^{-1}$  ( $\sigma_w = 5 \text{ cm s}^{-1}$ ),  $n_{\text{hom}} = 200 \text{ L}^{-1}$  ( $15 \text{ cm s}^{-1}$ ), and  $n_{\text{hom}} = 464 \text{ L}^{-1}$  ( $25 \text{ cm s}^{-1}$ ), exceeding the prescribed mean dust particle number concentration of  $28 \text{ L}^{-1}$ .

Table 1 summarizes ensemble statistics for each region. The large standard deviations (relative to the mean values) point to the huge variability of the data shown in Figure 6, caused by the wave-induced variability in  $w$  in concert with the strong dependence of homogeneously-nucleated ICNCs on updraft speed. In all updraft speed regimes, the mean ICNC stays well below the prescribed modal total dust number concentration (cat I), increases to this value (cat II), and increases further due to additional homogeneous freezing events (cat III). The latter

**Table 1**  
Ensemble Statistics (Rounded Values) Taken at Various Updraft Speed Standard Deviations,  $\sigma_w$ , Corresponding to the Simulations Shown in Figure 6

$\sigma_w$ [cm/s]	$n \pm \sigma_n$ [ $L^{-1}$ ]			$f$ [%]		
	5	15	25	5	15	25
cat I	$8 \pm 9$	$15 \pm 13$	$16 \pm 13$	93	65	48
cat II	$21 \pm 11$	$28 \pm 11$	$30 \pm 11$	4	14	15
cat III	$48 \pm 48$	$317 \pm 434$	$670 \pm 1005$	3	21	37
all data	$10 \pm 14$	$78 \pm 233$	$260 \pm 689$	100	100	100

Note. Mean nucleated ICNCs,  $n$ , Associated standard deviations,  $\sigma_n$ , and fractions of data points,  $f$ , in each category and across all data.

enhancement of mean ICNC is significant already in the low  $\sigma_w = 5 \text{ cm s}^{-1}$  case, although the spread of ICNC values is large. In about one out of five cases (21%) where cirrus clouds form at commonly observed mean updraft speed fluctuations ( $\sigma_w = 15 \text{ cm s}^{-1}$ ) in northern hemisphere background conditions, homogeneous freezing occurs mostly with reduced ICNC relative to pure homogeneous freezing (cat III). The majority of data points belong to cat I, with a decreasing trend as  $\sigma_w$  increases, indicating that partial activation of dust is prevalent in the upper troposphere.

We show in Appendix B that the activation curve for dust-enhanced situations is relatively similar to that used here to represent background conditions; however, the dust-enhanced total number concentration is about 10 times larger. If we repeated the calculations underlying Table 1, we would find fewer cat III entries, meaning that cirrus formation in situations with a high atmospheric dust load is controlled by heterogeneous nucleation.

We conclude this section by relating these results to data taken during the Midlatitude Cirrus Properties Experiment (MACPEX) (Jensen et al., 2013).

On average, wave-induced vertical wind speed variability ( $\sigma_w = 17 \text{ cm s}^{-1}$ ) caused a mean cirrus ICNC of  $90 \text{ L}^{-1}$ , well below values corresponding to pure homogeneous freezing (Kärcher et al., 2019). Repeating the above simulations, we find that  $n_{\text{tot}}$  values of  $35 \pm 15 \text{ L}^{-1}$  lead to a mean nucleated ICNC of  $96 \text{ L}^{-1}$  across all data points in the ensemble. While this result is in line with the aircraft measurements, actual dust INP numbers could be lower (leading to higher ICNCs due to an enhanced contribution of homogeneous freezing events), as the parameterization does not include ice crystal sedimentation (reducing observed ICNCs after nucleation) and we do not consider the possible presence of INPs other than dust.

Measurement-based estimates of cirrus ICNCs are available from remote sensing and in-situ observations (Gryspeerdt et al., 2018; Krämer et al., 2021; Mitchell et al., 2018; Sourdeval et al., 2018). Substantial uncertainties are caused by microphysical assumptions in retrieval algorithms affecting inferred cloud ice properties and the need to correct for shattering artifacts in cloud probes affecting  $\mu\text{m}$ -sized ice crystals counts. Moreover, optical array probe measurements suffer from uncertainties that are largest for small ice crystals owing to out-of-focus images and particle mis-sizing not associated with shattering.

That said, measured ICNCs show a wide range from 10 to 100s per liter of air, frequently showing signs of both homogeneous and heterogeneous ice nucleation. This is broadly consistent with the results shown in Table 1, implying that in view of ubiquitous variability in updraft speeds, potent INP such as mineral dust act to reduce homogeneously-produced ice numbers, at times suppressing homogeneous freezing thus limiting ICNCs down to some  $10 \text{ L}^{-1}$  or below.

#### 4. Summary

In the present study, an established parameterization scheme of cirrus ice formation is extended to include INPs based on approximate analytical solutions of the supersaturation equation for INPs and—building on former work—liquid solution droplets. Homogeneous freezing of solution droplets is allowed to compete with heterogeneous ice nucleation involving multiple INP types, based on measured or idealized activation spectra. The advanced scheme can also deal with pre-existing cirrus ice crystals and is computationally efficient. To facilitate applications, we discuss the use of the new scheme in (global) models. The outcome of predicted ice nucleation events is validated by comparison to more detailed numerical simulations.

Solving the supersaturation equation in closed form requires the use of constant deposition coefficients, which is an acceptable approximation for the transient nucleation stage. They should ideally be determined by comparison to more sophisticated nucleation and growth models that consider their supersaturation and size dependence. Future versions of the parameterization may include improved estimates of deposition coefficients and an explicit dependence of homogeneously-nucleated ice crystal numbers on the total number concentration of liquid solution droplets.

When adding dust INPs to aqueous solution droplets during cirrus formation events, predicted mean ICNCs come closer to values measured in the field. Using in-situ measurements of background mineral dust particle number

concentrations (on average  $28 \pm 12 \text{ L}^{-1}$ ) along with laboratory-generated ice activation data for desert dust, first applications of the parameterization for background conditions in the northern hemisphere show that partial or full activation of dust without homogeneous freezing occurs in about 4/5 of all cirrus formation events for a typically observed mean updraft speed. In the remaining cases, homogeneous freezing occurs but mostly with reduced total ICNCs relative to dust-free situations.

According to global-scale measurements, atmospheric abundances of mineral dust particles are highly variable with large regions containing only few ( $<1 - 10 \text{ L}^{-1}$ ) particles. Our estimates based on a log-normal distribution for total dust number concentrations do not fully reflect this variability. In global representations of dust-cirrus interactions, it is of equal importance to simulate both the presence and lack of dust INPs. In dust-poor regions, homogeneous freezing is more prevalent.

The improved parameterization scheme is also applied to aircraft-emitted soot particles, the large size fraction ( $>100 \text{ nm}$ ) of which has been shown in laboratory measurements to become ice-active below liquid water saturation by processing in contrails or mixed-phase clouds. As mineral dust particles nucleate cloud ice more efficiently and at lower ice supersaturation, it is conceivable that only in cases with low dust numbers and low updraft speeds might contrail-processed aviation soot particles compete with dust. This conjecture will be explored in future work.

A brief analysis of ice formation within cirrus shows that already some  $10 \text{ L}^{-1}$  of pre-existing cirrus ice crystals prevent ice nucleation at common mean updraft speeds  $10\text{--}20 \text{ cm s}^{-1}$  due to depositional growth, reinforcing earlier findings that total cirrus ICNC is a key parameter controlling new ice formation in cirrus. This holds provided that deposition coefficients for water vapor uptake on large cirrus ice crystals lie above about 0.1. Future studies may elucidate the updraft/ICNC conditions for ice nucleation within cirrus in the presence of interstitial INPs.

This work reports a significant improvement of our previous parameterization of cirrus cloud formation regarding the representation of INPs. More research is needed to investigate how different representations of wave-driven updrafts affect the role of INPs and the simulated global radiative forcing from aerosol-cirrus interactions. Mesoscale gravity waves are key to representing observed variability in vertical wind speeds. To drive the parameterization in global models with low spatial resolution, a subgrid-scale updraft speed model must be employed that properly accounts for this variability. We support recent findings regarding the role of mineral dust in cirrus formation with the use of only one typical mean updraft value constraining the updraft speed statistic. Nonetheless, more work is needed to better characterize mean updraft speeds as input to the parameterization in global model applications, as this crucial parameter generally exhibits substantial spatial and temporal variations.

## Appendix A: Pre-Existing Cirrus Ice Crystals

Nucleation of new ice crystals from interstitial INPs or solution droplets may also take place within cirrus clouds. Pre-existing cirrus ice crystals prevent new ice formation at a given updraft speed, if their deposition sink is strong enough to induce activation-relaxation before INPs start to activate or solution droplets freeze homogeneously. We explain how their effect is taken into account in the parameterization.

Pre-existing cirrus ice crystals (subscript ci) affect the potential new ice formation process via depositional growth. We characterize the cirrus ice crystals by total ICNC,  $n_{\text{ci}}$ , mean volume radius,  $r_{\text{ci}}$ , and deposition coefficient,  $\alpha_{\text{ci}}$ , as the minimum information needed to describe their effect. Their corresponding differential INP spectrum is given by

$$\frac{dn_{\text{ci}}}{ds} = n_{\text{ci}}\delta(s), \quad (\text{A1})$$

describing pulse activation at  $s = 0$ . Carrying out the  $s$ -integration in Equation 1 leads us to the deposition sink term:

$$\mathcal{L}_{\text{ci}} = \frac{4\pi s}{(vn_{\text{sat}})} \frac{b_{1,\text{ci}}}{b_{2,\text{ci}}^2} n_{\text{ci}} \mathcal{A}_{\text{ci}}(s), \quad (\text{A2})$$

with the corresponding activation-growth integral

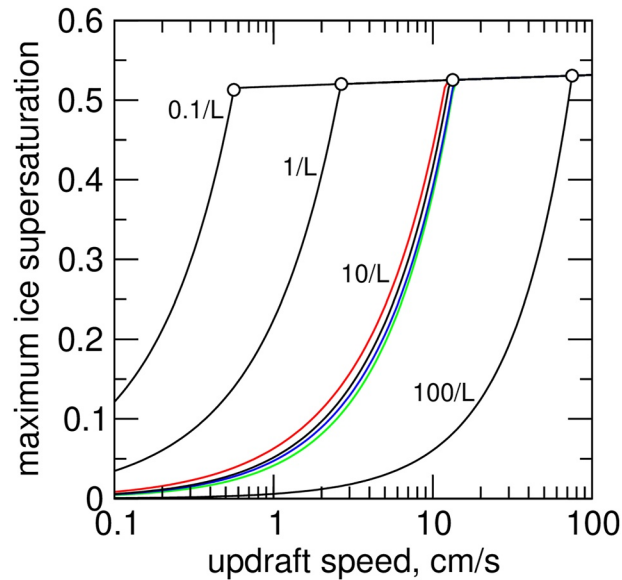


**Figure A1.** Maximum ice supersaturation at activation-relaxation in the presence of cirrus ice crystals with (black curves)  $r_{ci} = 30 \mu\text{m}$  and  $\alpha_{ci} = 0.1$  versus updraft speed. Labels indicate total cirrus ICNC,  $n_{ci}$ . Circles mark conditions where homogeneous freezing sets in. Sensitivity studies at  $n_{ci} = 10 \text{ L}^{-1}$  assume (red)  $r_{ci} = 20 \mu\text{m}$ , (green)  $r_{ci} = 40 \mu\text{m}$ , and (blue)  $\alpha_{ci} = 0.5$ .

$$\mathcal{A}_{ci}(s > 0) = \frac{\rho_{ci}^2(s, 0)}{1 + \rho_{ci}(s, 0)}, \quad \rho_{ci}(s, 0) = (1 + \delta_{ci}) \sqrt{1 + \kappa_{ci}s^2} - 1, \quad (\text{A3})$$

where the initial size parameter is given by  $\delta_{ci} = b_{2,ci}r_{ci}$  and the growth parameter,  $\kappa_{ci}$ , is based on Equation 18. Contrary to INPs,  $\delta_{ci}$  is larger than unity (depending on  $\alpha_{ci}$ ), as typically  $r_{ci} \gg r_{*}$ . That means that the growth of these ice crystals frequently takes place close to or in the diffusion-limited regime, while freshly nucleated ice crystals start growing in the kinetically-limited regime (Section 2.3).

Figure A1 shows as a function of updraft speed the maximum ice supersaturation,  $\hat{s}$ , attained in an air parcel containing pre-existing cirrus ice crystals with prescribed values for  $n_{ci}$ ,  $r_{ci} = 30 \mu\text{m}$ , and  $\alpha_{ci} = 0.1$ . The cirrus ice crystals quench the supersaturation before homogeneous freezing occurs, that is,  $\hat{s} < s_{\text{hom}}$ , up to critical updraft speeds (circles) that increase with  $n_{ci}$ . For higher  $w$ ,  $\hat{s} = s_{\text{hom}}$  varies only slightly with  $w$  (K22). If INPs were also present, they would activate into ice crystals only if the above maximum ice supersaturation was sufficiently high, implying large  $w$  for given  $n_{ci}$ .

Varying  $n_{ci}$  demonstrates that some  $10 \text{ L}^{-1}$  cirrus ice crystals prevent homogeneous freezing at mean updraft speeds around  $10\text{--}20 \text{ cm s}^{-1}$  that are frequently observed (Kärcher & Podglajen, 2019). Sensitivities due to variations in  $r_{ci}$  and  $\alpha_{ci}$  within the ranges indicated are small, revealing  $n_{ci}$  as the most crucial parameter controlling new ice formation in cirrus.

These findings are in general agreement with the treatment of pre-existing ice in, for example, the Community Atmosphere Model, showing that this effect has the potential to significantly reduce cirrus ICNCs (Shi et al., 2015). The relationship  $n_{ci}(w)$  connecting ICNCs of pre-existing cirrus in the absence of INPs with the updraft speed where homogeneous freezing commences (circles in Figure A1) is obtained by solving  $\mathcal{P} = \mathcal{L}_{ci}$  at  $s = s_{\text{hom}}$ :

$$n_{ci} = \frac{s_{\text{hom}} + 1}{s_{\text{hom}}} \frac{a_1 w}{\frac{4\pi}{v_{\text{sat}}} \frac{b_{ci1}}{b_{ci2}^2} \mathcal{A}_{ci}(s_{\text{hom}})}; \quad (\text{A4})$$

note that an additional  $w$ -dependence arises in the deposition term via  $\mathcal{A}_{ci}$  since  $\kappa_{ci} \propto 1/w$ . In the fast growth regime,  $\rho_{ci} \propto \sqrt{\kappa_{ci}} \gg 1$ , so that  $n_{ci} \propto w^{3/2}$ . In the slow growth regime,  $\mathcal{A}_{ci}$  no longer depends on  $w$ , so that the  $w$ -dependence arises from the forcing term alone:  $n_{ci} \propto w$ .

## Appendix B: Heterogeneous Ice Nucleation Spectra

Parameterizations of ice-active fractions based on laboratory measurements are available for single particles or monodisperse INP populations. Such parameterizations are arguable more difficult to infer from aircraft data. The supersaturation-dependent ice-active fractions are integrated over normalized particle number size distributions (PSDs) to yield deterministic INP spectra,  $\Phi(s)$ , analogous to  $s$ -cumulative condensation nuclei spectra (Ghan et al., 2011). We illustrate the estimation of such spectra based on special types of atmospherically relevant mineral dust and soot particles.

### B1. Desert Dust

Many types of atmospheric dust particles are good INPs and for some types, parameterizations of their ice activities are available. Recently, upper tropospheric dust PSDs were derived from global aircraft measurements during the Atmospheric Tomography Mission (ATom) (Froyd et al., 2022). Here we employ an activity parameterization for desert dust combined with an average and a perturbed dust PSD, representing northern hemisphere background ( $n_{\text{tot}} = 28 \text{ L}^{-1}$ ) and dust-enhanced ( $n_{\text{tot}} = 283 \text{ L}^{-1}$ ) conditions. The global ATom data set shows significant variability in  $n_{\text{tot}}$  for background dust ( $28 \pm 12 \text{ L}^{-1}$ ) with less pronounced variations in PSDs. While the use of a log-normal distribution to represent background conditions is technically correct, it may not be accurately representing most of the atmospheric samples taken during ATom (K. Froyd, personal communication, 2022). A large fraction of samples contain fewer than  $10 \text{ L}^{-1}$  or even  $1 \text{ L}^{-1}$  dust particles.

While the ATom measurements quantify the amount of dust composed of a variety of mineralogies (Froyd et al., 2019), we combine the PSDs with ice activities for desert dust. Therefore, the dust studied here activate like the nearly bare desert dust samples (organic content less than 20% by mass) studied in the laboratory (Ullrich et al., 2017).

Figure B1a shows the resulting spectrum,  $\Phi_{\text{dust}}$ . It is derived from empirically-determined, single particle ice activities depending on the particle surface area and the active site density,  $\eta(T, s)$  at  $T = 220 \text{ K}$ . The size-dependent ice-active fractions are integrated over the dust PSDs,  $df/dD$  (normalized to unity), based on spherical particles:

$$\Phi_{\text{dust}}(s) = \int_0^{\infty} [1 - \exp(-\pi D^2 \eta)] \frac{df}{dD} dD; \quad (\text{B1})$$

here,  $D$  is the diameter of a volume-equivalent sphere. The background and dust-enhanced spectra contain contributions from both, sub- $\mu\text{m}$  and super- $\mu\text{m}$  (up to about  $5 \mu\text{m}$ ) particles; the former constitute about 20–40% of the dust surface area and particles with sizes smaller than  $0.2 \mu\text{m}$  have negligible surface area. The spectra are quite similar, with the 50%-activation parameter near  $s = 0.37$  and activation occurring within the approximate range  $s = 0.3$ – $0.4$ ; full activation is already reached well below the homogeneous freezing threshold. The slightly better ice activity in the dust-enhanced case compared to the background case is due to a higher fraction of large coarse mode particles (relative to the fine mode) in the perturbed PSD (Froyd et al., 2022).

### B2. Aviation Soot

Soot particles are generally poor INPs, especially when coated with aqueous sulfuric acid solutions (Gao et al., 2021). Large (exceeding about  $200 \text{ nm}$  in size) soot particle aggregates form ice more efficiently after being processed in either mixed-phase clouds or contrails (Mahrt et al., 2020). Cloud processing leads to a compaction of the soot aggregates, enhancing their ice nucleation ability in the pore condensation and freezing mode (PCF). A physical parameterization of soot-PCF (Marcolli et al., 2021) has been applied to uncoated, contrail-processed aviation soot particles, yielding single particle ice-active fractions,  $\text{AF}(s, D_m)$ , valid around  $220 \text{ K}$  and for a contact angle of  $60^\circ$  at the soot-liquid water interface (Kärcher et al., 2021). The soot spectrum follows from

$$\Phi_{\text{soot}}(s) = \int_0^{\infty} \text{AF}(s, D_m) \frac{df}{dD_m} dD_m, \quad (\text{B2})$$

where  $D_m$  denotes the mobility diameter of the compacted soot aggregates and  $df/dD_m$  is the associated normalized size distribution. We employ log-normal parameters  $35.7 \text{ nm}$  and  $1.8$  for the modal mobility diameter and geometric standard deviation, respectively, representing an upper limit PSD and maximizing  $\Phi_{\text{soot}}$ , as discussed in

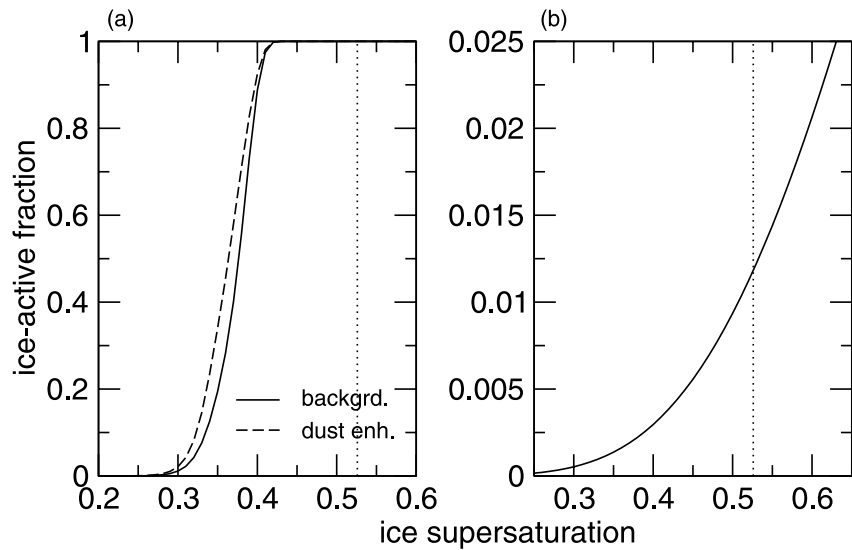


**Figure B1.** Ice-active fractions for (a) desert dust and (b) contrail-processed aviation soot particles as examples of good and poor atmospheric INPs (curves), respectively, based on detailed ice activity parameterizations. Underlying particle size distributions represent (solid) dust background and (dashed) dust-enhanced conditions and, in the case of soot, upper-limit conditions. Vertical dotted lines mark a value of the ice supersaturation threshold for homogeneous freezing-relaxation predicted by the parameterization for  $T = 220$  K and  $w = 15$  cm s<sup>-1</sup>.

Kärcher et al. (2021). Ice activity is dominated by particles >100 nm and particles smaller than about 40 nm are not ice-active according to soot-PCF. Figure B1b reveals that the onset of ice formation occurs as early as in the case of the dust particles, but increases very slowly with  $s$ . The upper-limit ice-active soot fraction at  $s_{\text{hom}}$  reaches only 1.2%, that is,  $\Phi_{\text{max}} \approx 0.012$ .

Total number concentrations of aviation soot particles depend on the time past emission from aircraft jet engines, or distance behind cruising aircraft, and whether they accumulate in overlapping plumes in dense aircraft corridors. A value roughly representing average conditions across upper tropospheric flight levels is  $n_{\text{tot}} = 500$  L<sup>-1</sup>, which implies  $n_{\star} = n_{\text{tot}} \Phi_{\text{max}} \approx 5.9$  L<sup>-1</sup>, a little higher than in the cloud model (Kärcher et al., 2021) due mainly to the slightly larger  $s_{\text{hom}}$ -value in the parameterization.

## Notation

$a$	thermodynamic parameter in Equation 1 (m <sup>-1</sup> )
$b_1$	ice growth parameter in Equation 4 (m·s <sup>-1</sup> )
$b_2$	ice growth parameter in Equation 4 (m <sup>-1</sup> )
$c_p$	specific heat of air at constant pressure (J·kg <sup>-1</sup> ·K <sup>-1</sup> )
$f$	fraction of data points
$g$	acceleration due to gravity (m·s <sup>-2</sup> )
$j$	index counting $J \geq 1$ distinct INP types
$n$	ice crystal number concentration deriving from INPs (m <sup>-3</sup> )
$n_{\star}$	INP number concentration ice-active at $s_{\text{hom}}$ (m <sup>-3</sup> )
$n_{\text{ci}}$	total number concentration of pre-existing cirrus ice crystals (m <sup>-3</sup> )
$n_{\text{d}}$	total number concentration of liquid solution droplets (m <sup>-3</sup> )
$n_{\text{hom}}$	ice crystal number concentration produced by homogeneous freezing (m <sup>-3</sup> )
$n_{\text{sat}}$	H <sub>2</sub> O number concentration at ice saturation (m <sup>-3</sup> )
$n_{\text{tot}}$	total INP number concentration (m <sup>-3</sup> )
$p$	air pressure (Pa)
$r$	volume-equivalent spherical ice crystal radius (m)
$r_{\text{ci}}$	initial mean volume radius of cirrus ice crystals (m)
$r_{\star}$	ice crystal core (dry INP) radius (m)

$s$	ambient ice supersaturation
$s_*$	location parameter of ice-active INP fraction
$\hat{s}$	ice supersaturation at heterogeneous activation-relaxation
$s_{\text{hom}}$	ice supersaturation at homogeneous freezing-relaxation
$s_+$	ice supersaturation where INPs start to activate
$s_-$	ice supersaturation where all INPs are ice-active
$t$	time (s)
$v$	mean thermal speed of H <sub>2</sub> O molecules in air (m·s <sup>-1</sup> )
$w$	vertical wind speed (m·s <sup>-1</sup> )
$w_{\downarrow}$	quenching velocity due to ice crystals derived from INPs (m·s <sup>-1</sup> )
$D$	diameter of a volume-equivalent sphere (m)
$D_m$	mobility diameter (m)
$D_v$	molecular diffusion coefficient for H <sub>2</sub> O in air (m <sup>2</sup> ·s <sup>-1</sup> )
$L$	enthalpy of sublimation (J·kg <sup>-1</sup> )
$T$	air temperature (K)
$R$	gas constant for air (J·kg <sup>-1</sup> ·K <sup>-1</sup> )
$R_v$	gas constant for water vapor (J·kg <sup>-1</sup> ·K <sup>-1</sup> )
$W$	effective vertical wind speed (m·s <sup>-1</sup> )
$\mathcal{A}$	activation-growth integral
$\mathcal{I}$	supersaturation integral in Equation 16 (s)
$\mathcal{L}$	production term in Equation 1 (s <sup>-1</sup> )
$\mathcal{P}$	production term in Equation 1 (s <sup>-1</sup> )
$\alpha$	(effective) deposition coefficient for uptake of H <sub>2</sub> O on ice crystals
$\delta$	initial ice crystal size parameter
$\eta$	active site density (m <sup>-2</sup> )
$\kappa$	ice crystal growth regime parameter
$\sigma$	standard deviation
$\rho$	scaled ice crystal radius
$\nu$	volume of an H <sub>2</sub> O molecule in bulk ice (m <sup>3</sup> )
$\omega$	quenching parameter separating activation and freezing regimes
$\Phi$	$s$ -cumulated ice-active INP fraction from theory or measurement
$\phi$	modeled $s$ -cumulated ice-active INP fraction bounded by 0 and one
$\tau_c$	cooling timescale (s)
$\tau_g$	timescale for radial ice crystal growth (s)
$\tau_q$	supersaturation quenching timescale (s)
$\delta s$	slope parameter of ice-active INP fraction
$\Delta s$	range of supersaturations where INPs are ice-active
$\Gamma$	absolute value of the dry adiabatic lapse rate (K·m <sup>-1</sup> )

## Data Availability Statement

The data that support the findings of this study are publicly available (Kärcher, 2022). A basic version of the parameterization is available upon reasonable request from the author.

## Acknowledgments

Fruitful discussions with Karl Froyd and Eric Jensen are gratefully acknowledged. In particular, I thank Karl Froyd for providing me with aircraft measurements of dust particle size distributions from the Atmospheric Tomography Mission. Open Access funding enabled and organized by Projekt DEAL.

## References

- Barahona, D., & Nenes, A. (2008). Parameterization of cirrus cloud formation in large-scale models: Homogeneous nucleation. *Journal of Geophysical Research*, 113. <https://doi.org/10.1029/2007JD009355>
- Barahona, D., & Nenes, A. (2009a). Parameterizing the competition between homogeneous and heterogeneous freezing in cirrus cloud formation. Monodisperse ice nuclei. *Atmospheric Chemistry and Physics*, 9, 369–381. <https://doi.org/10.5194/acp-9-369-2009>
- Barahona, D., & Nenes, A. (2009b). Parameterizing the competition between homogeneous and heterogeneous freezing in cirrus cloud formation. Polydisperse ice nuclei. *Atmospheric Chemistry and Physics*, 9, 5933–5948. <https://doi.org/10.5194/acp-9-5933-2009>
- Bock, L., & Burkhardt, U. (2016). The temporal evolution of a long-lived contrail cirrus cluster: Simulations with a global climate model. *Journal of Geophysical Research*, 121, 3548–3565. <https://doi.org/10.1002/2015JD024475>
- Dietlicher, R., Neubauer, D., & Lohmann, U. (2019). Elucidating ice formation pathways in the aerosol–climate model ECHAM6-HAM2. *Atmospheric Chemistry and Physics*, 19, 9061–9080. <https://doi.org/10.5194/acp-19-9061-2019>

- Dinh, T., Podglajen, A., Hertzog, A., Legras, B., & Plougonven, R. (2016). Effect of gravity wave temperature fluctuations on homogeneous ice nucleation in the tropical tropopause layer. *Atmospheric Chemistry and Physics*, *16*, 35–46. <https://doi.org/10.5194/acp-16-35-2016>
- Froyd, K. D., Murphy, D. M., Brock, C. A., Campuzano-Jost, P., Dibb, J. E., Jimenez, J.-L., et al. (2019). A new method to quantify mineral dust and other aerosol species from aircraft platforms using single-particle mass spectrometry. *Atmospheric Measurement Techniques*, *12*, 6209–6239. <https://doi.org/10.5194/amt-12-6209-2019>
- Froyd, K. D., Yu, P., Schill, G. P., Brock, C. A., Kupc, A., Williamson, C. J., et al. (2022). Dominant role of mineral dust in cirrus cloud formation revealed by global-scale measurements. *Nature Geoscience*, *15*, 177–183. <https://doi.org/10.1038/s41561-022-00901-w>
- Gao, K., Zhou, C.-W., Meier, E. J. B., & Kanji, Z. A. (2021). Ice nucleation activities of soot particles internally mixed with sulphuric acid at cirrus cloud conditions. *Atmospheric Chemistry and Physics*, *21*. <https://doi.org/10.5194/acp-2021-645>
- Gasparini, B., Blossy, P. N., Hartmann, D. L., Lin, G., & Fan, J. (2019). What drives the life cycle of tropical anvil clouds. *Journal of Advances in Modern Earth Systems*, *11*, 2586–2605. <https://doi.org/10.1029/2019MS001736>
- Gottelman, A., Liu, X., Ghan, S. J., Morrison, H., Park, S., Conley, A. J., et al. (2010). Global simulations of ice nucleation and ice super-saturation with an improved cloud scheme in the Community Atmosphere Model. *Journal of Geophysical Research*, *115*. <https://doi.org/10.1029/2009JD013797>
- Ghan, S. J., Abdul-Razzak, H., Nees, A., Ming, Y., Liu, X., Ovchinnikov, M., et al. (2011). Droplet nucleation: Physically-based parameterizations and comparative evaluation. *Journal of Advances in Modern Earth Systems*, *3*. <https://doi.org/10.1029/2011MS000074>
- Gryspeerd, E., Sourdeval, O., Quaas, J., Delanoë, J., Krämer, M., & Kühne, P. (2018). Ice crystal number concentration estimates from lidar-radar satellite remote sensing — Part 2: Controls on the ice crystal number concentration. *Atmospheric Chemistry and Physics*, *18*, 14351–14370. <https://doi.org/10.5194/acp-18-14351-2018>
- Harrington, J. Y., Moyle, A., Hanson, E., & Morrison, H. (2019). On calculating deposition coefficients and aspect ratio evolution in approximate models of ice crystal vapor growth. *Journal of the Atmospheric Sciences*, *76*, 1609–1625. <https://doi.org/10.1175/JAS-D-18-0319.1>
- Hendricks, J., Kärcher, B., & Lohmann, U. (2011). Effects of ice nuclei on cirrus clouds in a global climate model. *Journal of Geophysical Research*, *116*. <https://doi.org/10.1029/2010JD015302>
- Hoyle, C. R., Luo, B. P., & Peter, T. (2005). The origin of high ice crystal number densities in cirrus clouds. *Journal of the Atmospheric Sciences*, *62*, 2568–2579. <https://doi.org/10.1175/JAS3487.1>
- Jensen, E. J., Lawson, R. P., Bergman, J. W., Pfister, L., Bui, T. V., & Schmitt, C. G. (2013). Physical processes controlling ice concentrations in synoptically forced, midlatitude cirrus. *Journal of Geophysical Research*, *118*, 5348–5360. <https://doi.org/10.1002/jgrd.50421>
- Kanji, Z. A., Ladino, L. A., Wex, H., Boose, Y., Burkert-Kohn, M., Cziczo, D. J., & Krämer, M. (2017). Overview of ice nucleating particles. *Meteorological Monographs*, *58*, 1. <https://doi.org/10.1175/AMSMONOGRAPH5-D-16-0006.1>
- Kärcher, B. (2017a). Cirrus clouds and their response to anthropogenic activities. *Curr. Clim. Chang. Rep.*, *3*, 45–57. <https://doi.org/10.1007/s40641-017-0060-3>
- Kärcher, B. (2017b). Homogeneous ice formation in convective cloud outflow regions. *The Quarterly Journal of the Royal Meteorological Society*, *143*, 2093–2103. <https://doi.org/10.1002/qj.3069>
- Kärcher, B. (2022). A parameterization of cirrus cloud formation: Revisiting competing ice nucleation. [dataset]. Zenodo. Retrieved from <https://doi.org/10.5281/zenodo.6801033>
- Kärcher, B., DeMott, P. J., Jensen, E. J., & Harrington, J. Y. (2022). Studies on the competition between homogeneous and heterogeneous ice nucleation in cirrus formation. *Journal of Geophysical Research*, *127*. <https://doi.org/10.1029/2021JD035805>
- Kärcher, B., Hendricks, J., & Lohmann, U. (2006). Physically based parameterization of cirrus cloud formation for use in global atmospheric models. *Journal of Geophysical Research*, *111*. <https://doi.org/10.1029/2005JD006219>
- Kärcher, B., & Jensen, E. J. (2017). Microscale characteristics of homogeneous freezing events in cirrus clouds. *Geophysical Research Letters*, *44*. <https://doi.org/10.1002/2016gl072486>
- Kärcher, B., Jensen, E. J., & Lohmann, U. (2019). The impact of mesoscale gravity waves on homogeneous ice nucleation in cirrus clouds. *Geophysical Research Letters*, *46*, 5556–5565. <https://doi.org/10.1029/2019GL082437>
- Kärcher, B., & Lohmann, U. (2002a). A parameterization of cirrus cloud formation: Homogeneous freezing including effects of aerosol size. *Journal of Geophysical Research*, *107*, 9–1. <https://doi.org/10.1029/2001JD001429>
- Kärcher, B., & Lohmann, U. (2002b). A parameterization of cirrus cloud formation: Homogeneous freezing of supercooled aerosols. *Journal of Geophysical Research*, *107*. <https://doi.org/10.1029/2001JD000470>
- Kärcher, B., & Lohmann, U. (2003). A parameterization of cirrus cloud formation: Heterogeneous freezing. *Journal of Geophysical Research*, *108*. <https://doi.org/10.1029/2002JD003220>
- Kärcher, B., Mahrt, F., & Marcolli, C. (2021). Process-oriented analysis of aircraft soot-cirrus interactions constrains the climate impact of aviation. *Communications Earth & Environment*, *2*. <https://doi.org/10.1038/s43247-021-00175-x>
- Kärcher, B., & Marcolli, C. (2021). Aerosol-cloud interactions: The representation of ice activation in cloud models. *Atmospheric Chemistry and Physics*, *21*, 15213–15220. <https://doi.org/10.5194/acp-21-15213-2021>
- Kärcher, B., & Podglajen, A. (2019). A stochastic representation of temperature fluctuations induced by mesoscale gravity waves. *Journal of Geophysical Research*, *124*, 11506–11529. <https://doi.org/10.1029/2019JD030680>
- Köhler, C. G., & Seifert, A. (2015). Identifying sensitivities for cirrus modelling using a two-moment two-mode bulk microphysics scheme. *Tellus B: Chemical and Physical Meteorology*, *67*, 24494. <https://doi.org/10.3402/tellusb.v67.24494>
- Krämer, M., Rolf, C., Spelten, N., Afchine, A., Fahey, D., Jensen, E., et al. (2021). A microphysics guide to cirrus — Part 2: Climatologies of clouds and humidity from observations. *Atmospheric Chemistry and Physics*, *21*. <https://doi.org/10.5194/acp-20-12569-2020>
- Kuebbeler, M., Lohmann, U., Hendricks, J., & Kärcher, B. (2014). Dust ice nuclei effects on cirrus clouds. *Atmospheric Chemistry and Physics*, *14*, 3027–3046. <https://doi.org/10.5194/acp-14-3027-2014>
- Liu, X., & Penner, J. E. (2005). Ice nucleation parameterization for global models. *Meteorologische Zeitschrift*, *14*, 499–514. <https://doi.org/10.1127/0941-2948/2005/0059>
- Liu, X., Penner, J. E., Ghan, S. J., & Wang, M. (2007). Inclusion of ice microphysics in the NCAR community atmospheric model version 3 (CAM3). *Journal of Climate*, *20*, 4526–4547. <https://doi.org/10.1175/JCLI4264.1>
- Liu, X., & Shi, X. (2018). Sensitivity of homogeneous ice nucleation to aerosol perturbations and its implications for aerosol indirect effects through cirrus clouds. *Geophysical Research Letters*, *45*, 1684–1691. <https://doi.org/10.1002/2017GL076721>
- Lohmann, U., & Kärcher, B. (2002). First interactive simulations of cirrus clouds formed by homogeneous freezing in the ECHAM general circulation model. *Journal of Geophysical Research*, *107*, 8–1. <https://doi.org/10.1029/2001JD000767>
- Lohmann, U., Kärcher, B., & Timmreck, C. (2003). Impact of the mount pinatubo eruption on cirrus clouds formed by homogeneous freezing in the ECHAM4 GCM. *Journal of Geophysical Research*, *108*. <https://doi.org/10.1029/2002JD003185>

- Mahrt, F., Kilchhofer, K., Marcolli, C., Grönquist, P., David, R. O., Rösch, M., et al. (2020). The impact of cloud processing on the ice nucleation abilities of soot particles at cirrus temperatures. *Journal of Geophysical Research*, *125*. <https://doi.org/10.1029/2019JD030922>
- Marcolli, C., Mahrt, F., & Kärcher, B. (2021). Soot-PCF: Pore condensation and freezing framework for soot aggregates. *Atmospheric Chemistry and Physics*, *21*. <https://doi.org/10.5194/acp-2020-1134>
- Mitchell, D. L., Garnier, A., Pelon, J., & Erfani, E. (2018). CALIPSO (IIR-CALIOP) retrievals of cirrus cloud ice-particle concentrations. *Atmospheric Chemistry and Physics*, *18*, 17325–17354. <https://doi.org/10.5194/acp-18-17325-2018>
- Morrison, H., Lier-Walqui, M., Fridlind, A. M., Grabowski, W. W., Harrington, J. Y., Hoose, C., et al. (2020). Confronting the challenge of modeling cloud and precipitation microphysics. *J. Adv. Mod. Earth Sys.*, *12*. <https://doi.org/10.1029/2019MS001689>
- Muench, S., & Lohmann, U. (2020). Developing a cloud scheme with prognostic cloud fraction and two moment microphysics for ECHAM-HAM. *Journal of Advances in Modelling Earth Systems*, *12*. <https://doi.org/10.1029/2019MS001824>
- Murphy, D. M., & Koop, T. (2005). Review of the vapour pressures of ice and supercooled water for atmospheric applications. *The Quarterly Journal of the Royal Meteorological Society*, *131*, 1539–1565. <https://doi.org/10.1256/qj.04.94>
- Penner, J. E., Zhou, C., Garnier, A., & Mitchell, D. L. (2018). Anthropogenic aerosol indirect effects in cirrus clouds. *Journal of Geophysical Research*, *123*. <https://doi.org/10.1029/2018jd029204>
- Phillips, T. J. P., DeMott, P. J., & Andronache, C. (2008). An empirical parameterization of heterogeneous ice nucleation for multiple chemical species. *Journal of the Atmospheric Sciences*, *65*, 2757–2783. <https://doi.org/10.1175/2007jas2546.1>
- Podglajen, A., Hertzog, A., Plougonven, R., & Legras, B. (2016). Lagrangian temperature and vertical velocity fluctuations due to gravity waves in the lower stratosphere. *Geophysical Research Letters*, *43*, 3543–3553. <https://doi.org/10.1002/2016GL068148>
- Podglajen, A., Hertzog, A., Plougonven, R., & Legras, B. (2020). Lagrangian gravity wave spectra in the lower stratosphere of current (re)analyses. *Atmospheric Chemistry and Physics*, *20*, 9331–9350. <https://doi.org/10.5194/acp-20-9331-2020>
- Pruppacher, H. R., & Klett, J. D. (1998). *Microphysics of clouds and precipitation*. Kluwer Academic Publications.
- Ren, C., & MacKenzie, A. R. (2005). Cirrus parametrization and the role of ice nuclei. *The Quarterly Journal of the Royal Meteorological Society*, *131*, 1585–1605. <https://doi.org/10.1256/qj.04.126>
- Righi, M., Hendricks, J., Lohmann, U., Beer, C. G., Hahn, V., Heinold, B., et al. (2020). Coupling aerosols to (cirrus) clouds in the global EMAC-MADE3 aerosol-climate model. *Geoscientific Model Development*, *13*, 1635–1661. <https://doi.org/10.5194/gmd-13-1635-2020>
- Salzmann, M., Ming, Y., Golaz, J.-C., Ginoux, P. A., Morrison, H., Gettelman, A., et al. (2010). Two-moment bulk stratiform cloud microphysics in the GFDL AM3 GCM: Description, evaluation, and sensitivity tests. *Atmospheric Chemistry and Physics*, *10*, 8037–8064. <https://doi.org/10.5194/acp-10-8037-2010>
- Shi, X., Liu, X., & Zhang, K. (2015). Effects of pre-existing ice crystals on cirrus clouds and comparison between different ice nucleation parameterizations with the Community Atmosphere Model (CAM5). *Atmospheric Chemistry and Physics*, *15*, 1503–1520. <https://doi.org/10.5194/acp-15-1503-2015>
- Skrotzki, J., Connolly, P., Schnaiter, M., Saathoff, H., Möhler, O., Wagner, R., et al. (2013). The accommodation coefficient of water molecules on ice—Cirrus cloud studies at the AIDA simulation chamber. *Atmospheric Chemistry and Physics*, *13*, 4451–4466. <https://doi.org/10.5194/acp-13-4451-2013>
- Sourdeval, O., Gryspeerdt, E., Krämer, M., Goren, T., Delanoe, J., Afchine, A., et al. (2018). Ice crystal number concentration estimates from lidar-radar satellite remote sensing. *Atmospheric Chemistry and Physics*, *18*, 14327–14350. <https://doi.org/10.5194/acp-18-14327-2018>
- Squires, P. (1967). Cloud physics—Prose or poetry. *Bulletin of American Meteorological Society*, *48*. <https://doi.org/10.1175/1520-0477-48.6.400>
- Tully, C., Neubauer, D., Omanovic, N., & Lohmann, U. (2022). Cirrus cloud thinning using a more physically-based ice microphysics scheme in the ECHAM-HAM GCM. *Atmospheric Chemistry and Physics Discussions*, *22*. <https://doi.org/10.5194/acp-2021-685>
- Twomey, S. (1959). The nuclei of natural cloud formation Part II: The supersaturation in natural clouds and the variation of cloud droplet concentration. *Geofisica Pura e Applicata*, *43*, 243–249. <https://doi.org/10.1007/BF01993560>
- Ullrich, R., Hoose, C., Möhler, O., Niemand, M., Wagner, R., Höhler, K., et al. (2017). A new ice nucleation active site parameterization for desert dust and soot. *Journal of the Atmospheric Sciences*, *74*, 699–717. <https://doi.org/10.1175/JAS-D-16-0074.1>